JCTC Journal of Chemical Theory and Computation

Electric Field Gradients Calculated from Two-Component Hybrid Density Functional Theory Including Spin−Orbit Coupling

Fredy Aquino,[†] Niranjan Govind,[‡] and Jochen Autschbach*,[†]

Department of Chemistry, State University of New York at Buffalo, Buffalo, New York 14260-3000, and William R. Wiley Environmental Molecular Sciences Laboratory, Pacific Northwest National Laboratory, 902 Battelle Blvd, P.O. Box 999, Mail Stop K8-91 Richland, Washington 99352

Received May 30, 2010

Abstract: An implementation of a four-component density corrected approach for calculations of nuclear electric field gradients (EFGs) in molecules based on the two-component relativistic zeroth-order regular approximation (ZORA) is reported. The program module, which is part of the NWChem package, allows for scalar and spin−orbit relativistic computations of EFGs. Benchmark density functional calculations are reported for a large set of main group diatomic molecules, a set of Cu and Au diatomics, several Ru and Nb complexes, the free uranyl ion, and two uranyl carbonate complexes. Data obtained from nonhybrid as well as fixed and range-separated hybrid functionals are compared. To allow for a chemically intuitive interpretation of the results, a breakdown of the EFGs of selected systems in terms of localized molecular orbitals is given. For CuF, CuCl, AuCl, UO_2^{2+}, and a uranyl carbonate complex, the localized orbital decomposition demonstrates in particular the role of the valence metal d and f shells, respectively, and leads to rather compact analyses. For f orbitals, a Townes−Dailey-like model is set up to assist the analysis.

1. Introduction

In a molecule or in a crystal, a nuclear quadrupole moment interacts with the gradient of the electric field caused by the surrounding nuclei and electrons. This interaction is of high importance in experimental methods such as NMR,[1,2] NQR (nuclear quadrupole resonance),[1,3,4] Mössbauer spectroscopy,[5,6] and other high-resolution spectroscopic techniques. Quadrupolar coupling interactions are routinely observed in solution NMR spectra in the form of line broadening arising from relaxation mechanisms.[7] In solid-state NMR spectra, these interactions are found to dramatically alter spectral appearance. An extensive amount of work has been dedicated to the accurate calculation of nuclear quadrupole coupling parameters because of the importance of understanding their relationship with molecular structure.[8−11,2] From a quantum chemistry point of view, this structure−property relationship entails the accurate calculation of the electric field gradient (EFG).

The EFG is a molecular property that requires an all-electron treatment, at least for the atom of interest. When considering heavy atomic compounds, it is necessary to include relativistic effects in the calculations.[2,11] One way to include those effects is through four-component relativistic methods.[12] However, the usage of those methods tends to be limited to the study of small systems because they are computationally expensive. An efficient method for computing EFGs in "relativistic" molecular systems (e.g., systems containing heavy atoms) is a quasi-relativistic four-component density reconstructed electric field gradient method. Such a method was introduced by van Lenthe and Baerends[13] in the framework of the two-component zeroth-order regular approximation (ZORA) using density functional theory (DFT) and a Slater-type atomic orbital (STO) basis set. To

* To whom correspondence should be addressed. E-mail: jochena@buffalo.edu.

[†] State University of New York at Buffalo.

[‡] Pacific Northwest National Laboratory.

10.1021/ct1002847
Published on Web 08/10/2010

eliminate the bulk of picture-change effects, a reconstruction of the four-component electron density was proposed both in a scalar relativistic approximation (SRZ4) and in a variant including spin−orbit coupling (Z4). The approach was shown to provide reasonable results for EFG in a variety of molecules at an affordable computational expense. More recently, a similar approach has also been applied with ZORA and the two-component Douglas−Kroll−Hess (DKH) method using Gaussian type orbital (GTO) basis functions,[14] as well as explicit perturbation expansions of the DKH operator,[14,15] albeit only in a scalar relativistic framework. Among the available perturbative relativistic approaches, we mention an application of a scalar relativistic flavor of direct relativistic perturbation theory (DPT)[16,17] to calculations of EFGs in bromofluoromethane.[18]

The present work reports an implementation for EFG calculations within the Z4 and SR-Z4 frameworks, utilizing the recently developed ZORA module of the NWChem package,[19] which employs GTO basis sets for molecular calculations. The availability of this new implementation allows for the investigation of some questions regarding EFG calculations for main group elements and transition metals, among those the performance of the Z4 calculations in conjunction with range-separated hybrid functionals[20−22] in DFT that have recently been implemented in NWChem,[23,24] and the origin of the extreme sensitivity of copper and gold EFGs to approximations in the density functional.[25] We have developed a localized molecular orbital (LMO) analysis tool for field gradients to investigate the sensitivity of Cu and Au EFGs. The LMO analysis is also applied to study the effect of equatorial coordination on the uranium EFG in uranyl. Another aim of this paper is to test the suitability of various GTO basis set combinations for routine computations of heavy atom EFGs. Many of the previous works cited above used customized basis sets that are not readily available, for example, at the EMSL basis set exchange. We demonstrate by comparison with accurate literature data that suitable results—within typical error bars of DFT calculations—can be obtained for heavy atom EFGs with the basis sets used in this work, and that the LMO decomposition of EFGs leads to quite compact and chemically intuitive interpretations.

The paper is organized as follows: In section 2, the Z4 formalism for EFGs used for the implementation is outlined. Section 3 reports computational details and a few details about the program implementation. Results are presented and discussed in section 4 in the following order: main group diatomics, Cu and Au diatomics, complexes with Nb and Ru, and uranyl salts. Section 5 summarizes the findings.

2. Methodology

The electric field gradient (EFG) is evaluated from $\nabla \boldsymbol{E}(\boldsymbol{r})$ where the electric field is $\boldsymbol{E}(\boldsymbol{r}) = -\nabla\Phi(\boldsymbol{r})$. Here, $\Phi(\boldsymbol{r})$ is the electrostatic potential in an atom or molecule at point $\boldsymbol{r}$ caused by the distribution of charges (electrons, nuclei, and the surrounding of the system). Thus,

$$\mathrm{EFG}^{pq}(\boldsymbol{r}) = -\frac{\partial^2\Phi(\boldsymbol{r})}{\partial r_p \partial r_q} = -V_{pq}(\boldsymbol{r}) \tag{1}$$

where $r_p, r_q \in \{x, y, z\}$. The tensor $\mathbf{V}$ in its principal axis system, $V_{ij}(\boldsymbol{r})$ $(i, j \in \{1, 2, 3\})$, is a definition of the EFG often used by solid state NMR spectroscopists. The nuclear quadrupole coupling constant C_Q, for instance, is determined by V_{33}, which is the principal component with the largest magnitude. The conversion between C_Q in MHz and the EFG is $C_Q = 234.9647 Q V_{33}$, with the nuclear quadrupole moment Q here given in barn (1 barn $= 10^{-28}$ m^2) units and V_{33} in atomic units (a.u.). The electric potential $\Phi(\boldsymbol{r})$ has nuclear and electronic contributions:

$$\Phi(\boldsymbol{r}) = \Phi_{\mathrm{nuc}}(\boldsymbol{r}) + \Phi_{\mathrm{el}}(\boldsymbol{r}) \tag{2}$$

with $\Phi_{\mathrm{nuc}}(\boldsymbol{r})$ and $\Phi_{\mathrm{el}}(\boldsymbol{r})$ defined as

$$\Phi_{\mathrm{nuc}}(\boldsymbol{r}) = \sum_A \frac{Z_A}{|\boldsymbol{r} - \boldsymbol{R}_A|} \tag{3}$$

$$\Phi_{\mathrm{el}}(\boldsymbol{r}) = -\int \mathrm{d}^3 r' \frac{\rho(\boldsymbol{r}')}{|\boldsymbol{r} - \boldsymbol{r}'|} \tag{4}$$

in atomic units (au). Here, Z_A is a nuclear charge, $\boldsymbol{R}_{\mathrm{A}}$ is a nuclear center, and $\rho(\boldsymbol{r})$ is the electronic charge density.

Accordingly, the EFG has nuclear and electron contributions, where the nuclear term, $V_{pq}^{\mathrm{nuc}}(\boldsymbol{r})$, for point nuclei is

$$\begin{aligned} V_{pq}^{\mathrm{nuc}}(\boldsymbol{r}) &= \frac{\partial^2}{\partial r_p \partial r_q}\left(\sum_A \frac{Z_A}{|\boldsymbol{r} - \boldsymbol{R}_A|}\right) \\ &= \sum_A Z_A \hat{Q}_{pq}(\boldsymbol{r}, \boldsymbol{R}_A) \end{aligned} \tag{5}$$

and the electronic term, $V_{pq}^{el}(\boldsymbol{r})$, is

$$\begin{aligned} V_{pq}^{\mathrm{el}}(\boldsymbol{r}) &= \frac{\partial^2}{\partial r_p \partial r_q}\left(-\int \mathrm{d}^3 r' \frac{\rho(\boldsymbol{r}')}{|\boldsymbol{r} - \boldsymbol{r}'|}\right) \\ &= -\int \mathrm{d}^3 r' \rho(\boldsymbol{r}')\, \hat{Q}_{pq}(\boldsymbol{r}, \boldsymbol{r}') \end{aligned} \tag{6}$$

Here, the point quadrupole operator $\hat{Q}_{pq}(\boldsymbol{r},\boldsymbol{r}')$ is given as

$$\hat{Q}_{pq}(\boldsymbol{r}, \boldsymbol{r}') = \frac{3(r_p - r'_p)(r_q - r'_q) - \delta_{pq}(\boldsymbol{r} - \boldsymbol{r}')^2}{|\boldsymbol{r} - \boldsymbol{r}'|^5} \tag{7}$$

The expression for the electronic component of V_{pq} may also be derived within a perturbation theory framework, as a derivative of the electronic energy of the system with respect to the perturbation by a small point quadrupole Q located at position r, with the derivative taken at $Q = 0$. The perturbation operator is $-\hat{Q}_{pq}$. According to the Hellmann−Feynman theorem, the first-order perturbed energy is then $V_{pq}^{\mathrm{el}} = -\langle\Psi|\hat{Q}_{pq}|\Psi\rangle$ in wave function theories, leading to expression 6.

In Kohn−Sham DFT, where the electron density is parametrized as $\rho = \sum_i \varphi_i^\dagger \varphi_i$, the energy functional minimized in the Kohn−Sham procedure may be written as

$$\tilde{E} = \sum_i \varepsilon_i - E_C - \int d^3r \cdot (\rho V_{XC}) + E_{XC} - \sum_i \varepsilon_i \left(\sum_{\mu\nu} C^*_{\mu i} S_{\mu\nu} C_{\nu i} - 1 \right) \quad (8)$$

where E_C and E_{XC} are the Coulomb and exchange-correlation (XC) energy functionals, and V_{XC} is the XC potential. We assume canonical MOs where the Langrange multiplier ε_i is an eigenvalue of the Fock operator $\hat{F} = \hat{h} + V_C + V_{XC}$; that is, $\varepsilon_i = F_{ii} = \langle \varphi_i | \hat{F} | \varphi_i \rangle$. The last term with $S_{\mu\nu} = \langle \chi_\mu | \chi_\nu \rangle$ and the MO coefficients $C_{\mu i}$ ensures orthonormalization of the Kohn−Sham orbitals φ_i. Here and elsewhere, we assume single occupation of each molecular orbital (MO). Summation over spin indices is implied. A first order derivative of this functional with respect to a perturbation Q is

$$\frac{d\tilde{E}}{dQ} = \frac{\partial \tilde{E}}{\partial Q} + \sum_{\mu i} \frac{\partial \tilde{E}}{\partial C_{\mu i}} \cdot \frac{dC_{\mu i}}{dQ} = \frac{\partial \tilde{E}}{\partial Q} \quad (9)$$

since the energy is minimized with respect to variations of the MO coefficients. Thus, from eqs 8 and 9 for a basis set that is not dependent on the perturbation, one obtains

$$\frac{d\tilde{E}}{dQ} = \sum_i \frac{\partial \varepsilon_i}{\partial Q} = \sum_i \frac{\partial h_{ii}}{\partial Q} \quad (10)$$

With $-\hat{Q}_{pq}$ substituted for the operator derivative, the right-hand side yields eq 6. The definition of the EFG via a sum of orbital energy derivatives is used below when the scaled ZORA orbital energies are defined.

The equation for the electronic term of the EFG implies that ρ is the correct electronic charge density. This is the case in nonrelativistic theory, and in four-component relativistic methods. In the present work, we base the EFG calculations on the quasi-relativistic two-component ZORA method where the Kohn−Sham equations read

$$\left[(\boldsymbol{\sigma} \cdot \hat{\boldsymbol{p}}) \frac{\hat{K}}{2} (\boldsymbol{\sigma} \cdot \hat{\boldsymbol{p}}) + V(\boldsymbol{r}) \right] \varphi_i = \varepsilon_i^{\mathrm{ZORA}} \varphi_i \quad (11)$$

with

$$\hat{K} = \frac{2c^2}{2c^2 - V} \quad (12)$$

The vector spin operator is $\boldsymbol{\sigma} = \sigma_x \hat{\boldsymbol{x}} + \sigma_y \hat{\boldsymbol{y}} + \sigma_z \hat{\boldsymbol{z}}$. The σ_k ($k = x, y, z$) are the Pauli matrices, the linear momentum is given by $\hat{\boldsymbol{p}} = -i\nabla$, and the two-component molecular spinors $\varphi_i(\boldsymbol{r})$ are

$$\varphi_i(\boldsymbol{r}) = \sum_\mu \chi_\mu(\boldsymbol{r}) \begin{pmatrix} C^{\alpha}_{\mu i} \\ C^{\beta}_{\mu i} \end{pmatrix} = \begin{pmatrix} \varphi_i^{\alpha}(\boldsymbol{r}) \\ \varphi_i^{\beta}(\boldsymbol{r}) \end{pmatrix} \quad (13)$$

In the implementation used for the present work, the $\chi_\mu(\boldsymbol{r})$ are Gaussian-type AO basis functions (GTOs). The potential V includes the nuclear electron, the Coulomb, and the XC potential. In our implementation, V used in eq 12 is based on an electron density calculated at the Hartree−Fock (HF) level[19] and excludes XC terms (unlike some other ZORA implementations[26−28]). This approximation has been carefully benchmarked in ref 19 and will be validated further in this work by comparisons of calculated EFGs with literature data.

The two-component electron density $\rho^Z = \sum_i \varphi_i^\dagger \varphi_i$ is not the charge density,[29] leading to picture-change errors in the calculated EFG.[13−15,30,31] Van Lenthe and Baerends suggested reconstructing a normalized four-component electron charge density from the ZORA orbitals for the purpose of EFG computations in order to eliminate most of the picture-change errors in order c^{-2}. The electronic part of the EFG can be obtained from a four-component (Dirac) electron density, $\rho^D(\boldsymbol{r}) = \sum_i (U^\dagger \varphi_i(\boldsymbol{r}))^\dagger (U^\dagger \varphi_i(\boldsymbol{r}))$, where U is the Foldy−Wouthuysen unitary transformation.[13,32] From using an approximation of U consistent with ZORA, the electron charge density is reconstructed, $\rho^D(\boldsymbol{r}) \approx \rho^{Z4}(\boldsymbol{r})$. The quasi-relativistic corrected normalized electron density, $\rho^{Z4}(\boldsymbol{r})$ in the context of ZORA is given by[13]

$$\rho^{Z4}(\boldsymbol{r}) = \sum_{i=1}^{\mathrm{occ}} \frac{\rho_i^Z(\boldsymbol{r}) + \rho_i^S(\boldsymbol{r})}{1 + S_i} \quad (14)$$

where

$$S_i = \langle \varphi_i | (\boldsymbol{\sigma} \cdot \hat{\boldsymbol{p}}) \hat{B} (\boldsymbol{\sigma} \cdot \hat{\boldsymbol{p}}) | \varphi_i \rangle \quad (15)$$

and

$$\hat{B} = \frac{c^2}{[2c^2 - V]^2} \quad (16)$$

Here, the ZORA electron density, $\rho_i^Z(\boldsymbol{r})$, and the "small component" density, $\rho_i^S(\boldsymbol{r})$, for each MO are

$$\rho_i^Z(\boldsymbol{r}) = \varphi_i^\dagger(\boldsymbol{r})\, \varphi_i(\boldsymbol{r}) \quad (17)$$

$$\rho_i^S(\boldsymbol{r}) = (\boldsymbol{\sigma} \cdot \hat{\boldsymbol{p}} \varphi_i)^\dagger\, \hat{B} (\boldsymbol{\sigma} \cdot \hat{\boldsymbol{p}}) \varphi_i \quad (18)$$

It is beneficial to adopt the "scaled ZORA" approach.[33,34] The ZORA orbitals are usually excellent approximations of fully relativistic orbitals for valence and outer-core shells. However, orbital energies and properties calculated from the ZORA orbitals are very different from the fully relativistic results for core orbitals in heavy atoms. Van Lenthe and Baerends have shown that the orbital energies can be significantly improved toward the fully relativistic values upon applying of a scaling factor

$$\varepsilon_i^{\text{scaled-ZORA}} = \frac{\varepsilon_i^{\mathrm{ZORA}}}{1 + S_i} \quad (19)$$

where S_i is the same term as in eq 15. Application of eq 10 with the *scaled* ZORA energies to derive the electronic EFG contribution leads to an EFG expression as in eq 6 with ρ replaced by the Z4 density (eq 14). Thus, the electronic term, $V_{pq}^{\mathrm{el}}(\boldsymbol{r})$, reads in the Z4 method

$$V_{pq}^{\mathrm{el}}(\boldsymbol{r}) = -\int d^3r' \rho^{Z4}(\boldsymbol{r}')\, \hat{Q}_{pq}(\boldsymbol{r}, \boldsymbol{r}') = -I_{pq}^Z(\boldsymbol{r}) - I_{pq}^S(\boldsymbol{r}) \quad (20)$$

In eq 20, $I_{pq}^Z(\boldsymbol{r})$ is given by

$$I^{Z}_{pq}(\boldsymbol{r}) = \sum_{\mu\nu} P'_{\mu\nu} \int \mathrm{d}^3 r' \chi_\mu(\boldsymbol{r}') \chi_\nu(\boldsymbol{r}') \hat{Q}_{pq}(\boldsymbol{r}, \boldsymbol{r}') \quad (21)$$

where $P'_{\mu\nu}$ represents a scaled density matrix:

$$P'_{\mu\nu} = \sum_{i=1}^{\mathrm{occ}} \frac{C^{\alpha^*}_{\mu i} C^{\alpha}_{\nu i} + C^{\beta^*}_{\mu i} C^{\beta}_{\nu i}}{1 + S_i} \quad (22)$$

The MO integrals needed in eq 21 can be evaluated analytically in the AO basis in terms of Boys functions[35] or Rys polynomials[36] by standard procedures.[37−41]

In eq 20, the term $I^{S}_{pq}(\boldsymbol{r})$ related to the small component density and the scaled-ZORA scaling factor can be calculated as

$$\begin{aligned} I^{S}_{pq}(\boldsymbol{r}) = & \\ & \sum_{\mu,\nu} P'_{\mu\nu} \sum_k \left\langle \frac{\partial \chi_\mu}{\partial r'_k} \middle| \hat{B} \hat{Q}_{pq}(\boldsymbol{r}, \boldsymbol{r}') \middle| \frac{\partial \chi_\nu}{\partial r'_k} \right\rangle + \\ & \sum_{\mu,\nu} P'_{x,\mu\nu} \left(\left\langle \frac{\partial \chi_\mu}{\partial y'} \middle| \hat{B} \hat{Q}_{pq}(\boldsymbol{r}, \boldsymbol{r}') \middle| \frac{\partial \chi_\nu}{\partial z'} \right\rangle - \right. \\ & \left. \left\langle \frac{\partial \chi_\mu}{\partial z'} \middle| \hat{B} \hat{Q}_{pq}(\boldsymbol{r}, \boldsymbol{r}') \middle| \frac{\partial \chi_\nu}{\partial y'} \right\rangle \right) + \\ & \sum_{\mu,\nu} P'_{y,\mu\nu} \left(\left\langle \frac{\partial \chi_\mu}{\partial z'} \middle| \hat{B} \hat{Q}_{pq}(\boldsymbol{r}, \boldsymbol{r}') \middle| \frac{\partial \chi_\nu}{\partial x'} \right\rangle - \right. \\ & \left. \left\langle \frac{\partial \chi_\mu}{\partial x'} \middle| \hat{B} \hat{Q}_{pq}(\boldsymbol{r}, \boldsymbol{r}') \middle| \frac{\partial \chi_\nu}{\partial z'} \right\rangle \right) + \\ & \sum_{\mu,\nu} P'_{z,\mu\nu} \left(\left\langle \frac{\partial \chi_\mu}{\partial x'} \middle| \hat{B} \hat{Q}_{pq}(\boldsymbol{r}, \boldsymbol{r}') \middle| \frac{\partial \chi_\nu}{\partial y'} \right\rangle - \right. \\ & \left. \left\langle \frac{\partial \chi_\mu}{\partial y'} \middle| \hat{B} \hat{Q}_{pq}(\boldsymbol{r}, \boldsymbol{r}') \middle| \frac{\partial \chi_\nu}{\partial x'} \right\rangle \right) \end{aligned} \quad (23)$$

where partial integration has been applied to avoid derivatives of $\hat{B}$. In the last equation, $P'_{x,\mu\nu}$, $P'_{y,\mu\nu}$, and $P'_{z,\mu\nu}$ are scaled spin-density matrices given by

$$P'_{x,\mu\nu} = i \sum_{i=1}^{\mathrm{occ}} \frac{C^{\alpha^*}_{\mu i} C^{\beta}_{\nu i} + C^{\beta^*}_{\mu i} C^{\alpha}_{\nu i}}{1 + S_i} \quad (24)$$

$$P'_{y,\mu\nu} = \sum_{i=1}^{\mathrm{occ}} \frac{C^{\alpha^*}_{\mu i} C^{\beta}_{\nu i} - C^{\beta^*}_{\mu i} C^{\alpha}_{\nu i}}{1 + S_i} \quad (25)$$

$$P'_{z,\mu\nu} = i \sum_{i=1}^{\mathrm{occ}} \frac{C^{\alpha^*}_{\mu i} C^{\alpha}_{\nu i} - C^{\beta^*}_{\mu i} C^{\beta}_{\nu i}}{1 + S_i} \quad (26)$$

Those matrices have the property

$$P'^{*}_{k,\nu\mu} = -P'_{k,\mu\nu} \quad k = x, y, z \quad (27)$$

which can be used to prove that $I^{S}_{pq}(\boldsymbol{r})$ is a real quantity, as it should be.

The EFG from scalar relativistic ZORA is obtained by neglecting spin-dependent terms in the ZORA Kohn−Sham operator and in the EFG related integrals. The scaling integral, S_i, is redefined in the following way:

$$\begin{aligned} S_i &= \langle \varphi_i | (\boldsymbol{\sigma} \cdot \hat{\boldsymbol{p}}) \hat{B} (\boldsymbol{\sigma} \cdot \hat{\boldsymbol{p}}) | \varphi_i \rangle \\ &= \langle \varphi_i | \hat{\boldsymbol{p}} \hat{B} \hat{\boldsymbol{p}} + i \boldsymbol{\sigma} \cdot (\hat{\boldsymbol{p}} \hat{B} \times \hat{\boldsymbol{p}}) | \varphi_i \rangle \\ S^{\mathrm{ZORA}}_{\mathrm{SR},i} &= \langle \varphi_i | \hat{\boldsymbol{p}} \hat{B} \hat{\boldsymbol{p}} | \varphi_i \rangle \end{aligned} \quad (28)$$

As a consequence of the redefinition of the small component density, $\rho^{S}_{i}(\boldsymbol{r})$, the expression for $I^{S}_{pq}(\boldsymbol{r})$ is approximated as

$$I^{S}_{pq}(\boldsymbol{r}) \approx \sum_{\mu,\nu} P'_{\mu\nu} \sum_k \left\langle \frac{\partial \chi_\mu}{\partial r'_k} \middle| \hat{B} \hat{Q}_{pq}(\boldsymbol{r}, \boldsymbol{r}') \middle| \frac{\partial \chi_\nu}{\partial r'_k} \right\rangle \quad (29)$$

with $P'_{\mu\nu}$ now calculated with the scalar relativistic S_i from eq 28. The scalar relativistic $I^{Z}_{pq}(\boldsymbol{r})$ is calculated from eq 21 using the scalar relativistic $P'_{\mu\nu}$ terms.

3. Computational and Implementation Details

The quasi-relativistic EFG has been added to the recently implemented ZORA code reported by Nichols et al.[19] in the NWChem 5.1 package.[42−44] NWChem previously had a spin-free module for the evaluation of electric field gradients which used as electronic density $\rho^{Z}(\boldsymbol{r}) = \sum_i^{\mathrm{occ}} \rho^{Z}_i(\boldsymbol{r})$. For this work, we added picture-change corrections,[13] by choosing $\rho^{Z4}(\boldsymbol{r})$, eq 14, and extended the EFG module for spin−orbit Z4 computations.

The implementation of quasi-relativistic corrections to the EFG involved (i) evaluation of the scaled density matrices $P'_{\mu\nu}$, $P'_{x,\mu\nu}$, $P'_{y,\mu\nu}$, and $P'_{z,\mu\nu}$; (ii) evaluation of eq 21, $I^{Z}_{pq}(\boldsymbol{r})$; (iii) numerical computation of the integrals in eq 23, which allows for the evaluation of $I^{S}_{pq}(\boldsymbol{r})$. The evaluation of those integrals depends on the use of a reliable molecular integration grid. The grid was checked for the set of all diatomics by calculating the integrals of eq 21 analytically and by numerical integration. The results agreed within 5×10^{-3} relative error for the electronic component of V_{33} in the worst case (AuBr ZORA-4 CAM-B3LYP), and within 9×10^{-5} relative error on average. The evaluation of the electronic component of the EFG, $V^{\mathrm{el}}_{pq}(\boldsymbol{r})$, followed steps i, ii, and iii; from there, $V_{pq}(\boldsymbol{r})$ was computed. The new module allows for two types of calculations: (a) restricted and unrestricted scalar relativistic ZORA: the module determines the EFG for scalar relativistic ZORA along with Z4 corrections (SR-Z4), suited for studying closed and open shell molecular systems; (b) spin−orbit ZORA and the associated Z4 corrections.

For the evaluation of the corrected electric field gradients at the heavy atom centers of interest, a choice of basis set with the following characteristics was adopted. (a) We chose a relativistic atomic GTO basis set that has the flexibility to include relativistic effects in the evaluation of the EFG integrals and is able to describe relativistic effects on the MOs. (b) Valence polarization functions were added where needed. The polarization functions were taken from the (def2) TZVPP[45] basis set available at the EMSL basis set exchange.[46,47] (c) For increased flexibility in the core, the basis sets for the EFG atom were uncontracted. The basis sets chosen in this way represent a relatively economic choice

for routine EFG computations, somewhat similar in flexibility to the uncontracted Slater-type orbital (STO) basis sets chosen by van Lenthe and Baerends for their ZORA EFG computations.[13,48]

For the section that validates the implementation with calculations of EFGs in diatomic molecules, we uncontracted the basis set from Tsuchiya−Abe−Nakajima−Hirao[49] (TANH) and added polarization functions from TZVPP. This basis set was also used for the calculation of EFGs in the copper diatomics. For the calculation of EFGs in gold diatomics, we used the SARC-ZORA TZVPP basis[50] for the Au atom and the uncontracted version of the TANH basis set along with polarization functions from TZVPP for all other atoms. In the "applications" sections, the basis sets used for the metal complexes were as follows: (i) ANO-RCC[51] was used for ruthenium and niobium along with the 6-31G* basis set for ligand atoms. (ii) For comparison, calculations were also performed with the uncontracted TANH basis set polarized with TZVPP for Nb, and some comparisons were made by varying the ligand basis set as detailed in that section. (iii) For the uranium systems, we used the ANO-RCC basis set excluding *h* functions (see the section on metal complexes for benchmarks), along with TZVPP and 6-31G* for the ligand atoms. Some benchmark calculations in section 4.1 have also been carried out with the ANO basis set for heavy main group atoms because of convergence problems with the uncontracted TANH basis for At.

For the validation tests of EFGs for diatomic halides as well as the Cu and Au diatomics, we investigated the performance of the following functionals: Becke88[52]+Perdew86[53] (BP), Becke88[52]+LYP[54] (BLYP), Becke three-parameter Lee−Yang−Parr (B3LYP),[55] and two parametrizations of the Coulomb-attenuated (range-separated) version of B3LYP:[21] CAM-B3LYP-A is the original parametrization with $\alpha + \beta = 0.65$, while CAM-B3LYP-B uses $\alpha + \beta = 1$ and is therefore fully long-range-corrected. We have also tested another parametrization of CAM-B3LYP which was optimized for EFG calculations on copper, CAM-B3LYP*.[56] For the study of larger systems, namely, the ruthenium, niobium, and uranium complexes, we used CAM-B3LYP-A, B3LYP, and revPBE.[57−59] The revPBE and B3LYP functionals were chosen to facilitate a comparison with literature data for the Nb and Ru EFGs, and the comparison with CAM-B3LYP allows for an assessment of the performance of a range-separated functional for EFGs in these larger metal complexes.

For the localized orbital analysis of the EFGs, the following sequence of SR-Z4 calculations was employed in scalar relativistic calculations:

(i) The EFG tensor (electronic plus nuclear contributions) was calculated and the principal axis system (PAS) determined.

(ii) AO matrix elements used for the calculation of I^Z_{pq} and I^S_{pq} in eq 20 were combined. Corresponding EFG AO matrix elements for the *nuclear* EFG contributions were calculated from the AO overlap matrix, and from the AO matrix elements used to calculate the scalar relativistic S_i of eq 15, both scaled with V^{nuc}_{pq}/N. The electronic and "nuclear" AO matrices were added to yield an AO matrix $h^{pq}_{\mu\nu}$ which yields the full (electronic plus nuclear) EFG tensor in the laboratory frame upon contraction with $P'_{\mu\nu}$ of eq 22.

(iii) The $h^{pq}_{\mu\nu}$'s were transformed to the PAS to yield $h^{11}_{\mu\nu}$, $h^{22}_{\mu\nu}$, and $h^{33}_{\mu\nu}$. For highly symmetric molecules, this is not necessary, but it considerably simplifies the analysis for systems where the PAS does not coincide with the laboratory coordinates.

(iv) The NBO 5.0 code version 5.0[60] was used to create a set of scalar relativistic natural localized MOs (NLMOs) and natural bond orbitals (NBOs). The columns of the NLMO to MO transformation matrix were scaled with the S_i, and the result was used together with the MO coefficients and the AO to NBO transformation to partition the principal components of the EFG tensor into contributions from individual NLMOs or NBOs. We refer the reader to refs 2, 61, and 62 for further details about the NBO/NLMO analysis of EFG tensors and other molecular properties. The implementation was originally carried out within the Amsterdam Density Functional package. For the purpose of this work, the analysis code has been turned into a stand-alone program that reads as input the AO matrices $h^{11}_{\mu\nu}$, $h^{22}_{\mu\nu}$, and $h^{33}_{\mu\nu}$; the scaling factors S_i; the MO coefficients and the AO overlap matrix; and a set of matrices generated by the NBO program (transformations between NLMOs and MOs and between AOs and NBOs).

4. Results and Discussion

In this section, the implementation of the corrected electric field gradients in NWChem is validated by comparing a set of calculations on diatomic halides as well as Cu and Au diatomics with literature data. As an application to larger systems, we compute metal Z4 EFGs of a set of ruthenium, niobium, and uranium complexes. The results for these systems are going to be compared with previous calculations performed at the nonhybrid DFT level.

4.1. Test Set 1: Diatomic Main Group Halides. Table 1 lists EFGs at halides using the BP functional for SR ZORA, SR-Z4, ZORA, and Z4. The BP functional was used because of the availability of literature data with this functional from two different sources. The EFGs are in good agreement with the corresponding values in parentheses taken from the work of Neese et al.[14] for F and At and from the work of van Lenthe and Baerends[13] for the other molecules. Minor differences must be expected mainly because of the different basis sets used, and because of the different numerical integration grids applied in the DFT calculations. On a more technical level, there are also differences in how the potential V is included in the ZORA operator $\hat{K}$ in eq 12, but prior benchmarks[19,63,64] have indicated that the approximations in V made to construct $\hat{K}$ are not overly critical beyond inclusion of the nuclear potential and a per atom electronic Coulomb potential.

In all cases, the sign and magnitude of the Z4 correction terms calculated for this work are in agreement with the literature data. The sign and magnitude of the spin−orbit

Table 1. Calculated Electric Field Gradient, V_{33}, at F, Cl, Br, I, and At in Hydrogen Halides and TlI[a]

	SR ZORA		SR-Z4		ZORA		Z4	
HF	2.7654	(2.7826)	2.7638	(2.7806)	2.7654		2.7638	
HCl	3.5561	(3.5627)	3.5481	(3.5481)	3.5562	(3.5627)	3.5485	(3.5533)
HBr	7.5752	(7.6182)	7.4569	(7.4706)	7.5835	(7.6295)	7.4970	(7.5430)
HI[b]	11.5014	(11.5959)	11.0035	(11.0470)	11.5556	(11.6700)	11.2335	(11.3369)
HAt	25.1128	(25.4477)	22.1853	(22.5743)	25.4021		23.4414	
TlI[b]	2.2887	(2.3118)	2.1903	(2.2032)	2.7366	(2.7855)	2.7000	(2.7491)

[a] BP functional, ANO-RCC basis for heavier atoms, and TZVPP for hydrogen. EFGs in parentheses are from the work of Neese et al.[14] for F and At and from van Lenthe and Baerends[13] for Cl, Br, and I. [b] For comparison, the results with the TANH basis (see section 3 and Table 2) are, for HI, SR-Z4 = 11.0590 and Z4 = 11.2893, and for TlI, SRZ4 = 2.1881 and Z4 = 2.6987.

Table 2. Calculated Electric Field Gradient, V_{33}, at the Halide Nucleus for a Set of Diatomics[a]

		NR		SR-Z4		Z4		observed
AlCl	^{35}Cl	0.4168	(0.4153)	0.4206	(0.4193)	0.4207	(0.4201)	0.4602[b]
GaCl	^{35}Cl	0.6576	(0.6536)	0.6667	(0.6630)	0.6684	(0.6662)	0.6880[c]
InCl	^{35}Cl	0.6831	(0.6807)	0.7043	(0.7021)	0.7160	(0.7151)	0.6933[c]
CuCl	^{35}Cl	2.2801	(2.0798)	2.4885	(2.2909)	2.4889	(2.2945)	1.675[b]
HCl	^{35}Cl	3.5427	(3.5038)	3.5865	(3.5481)	3.5870	(3.5533)	3.516[d]
ICl	^{35}Cl	4.5996	(4.5656)	4.6844	(4.6453)	4.5697	(4.5353)	4.472[d]
BrCl	^{35}Cl	5.3737	(5.3375)	5.4355	(5.3975)	5.4159	(5.3845)	5.336[d]
AlBr	^{79}Br	0.9444	(0.9695)	1.0113	(1.0324)	1.0154	(1.0463)	1.112[e]
GaBr	^{79}Br	1.3133	(1.3335)	1.3995	(1.4130)	1.4086	(1.4343)	1.50[c]
InBr	^{79}Br	1.3784	(1.3988)	1.4848	(1.4981)	1.5172	(1.5407)	1.57[c]
CuBr	^{79}Br	4.5031	(4.2631)	5.1641	(4.9029)	5.1731	(4.9454)	3.71[f]
HBr	^{79}Br	7.0599	(7.0394)	7.5154	(7.4706)	7.5424	(7.5430)	7.55[d]
IBr	^{79}Br	9.3799	(9.3957)	9.9862	(9.9575)	9.8467	(9.8767)	9.89[c]
BrCl	^{79}Br	11.6139	(11.6457)	12.2909	(12.2841)	12.2761	(12.3437)	12.4[d]
AlI	^{127}I	1.4295	(1.4532)	1.6899	(1.7011)	1.7289	(1.7511)	1.90[c]
GaI	^{127}I	1.7598	(1.7869)	2.0515	(2.0706)	2.1024	(2.1348)	2.28[c]
InI	^{127}I	1.8682	(1.8911)	2.1862	(2.1884)	2.2763	(2.2914)	2.38[c]
TlI	^{127}I	1.8774	(1.8979)	2.1881	(2.2032)	2.6987	(2.7491)	2.70[c]
CuI	^{127}I	6.2237	(5.9213)	7.7206	(7.3770)	7.7909	(7.4942)	5.79[f]
HI	^{127}I	9.5711	(9.5913)	11.0590	(11.0470)	11.2893	(11.3369)	11.3[d]
IBr	^{127}I	14.7489	(14.8218)	16.8048	(16.8388)	16.7654	(16.8696)	16.8[d]
ICl	^{127}I	15.7324	(15.8272)	17.9269	(17.9799)	17.7673	(17.8874)	18.1[d]
IF	^{127}I	18.4959	(18.6275)	21.0265	(21.1071)	20.7241	(20.8850)	21.2[d]
AlF	^{27}Al	−1.1148	(−1.1032)	−1.1194	(−1.1075)	−1.1194	(−1.1078)	−1.096[c]
AlCl	^{27}Al	−0.9199	(−0.9087)	−0.9221	(−0.9107)	−0.9221	(−0.9110)	−0.8828[c]
AlBr	^{27}Al	−0.8546	(−0.8436)	−0.8511	(−0.8402)	−0.8504	(−0.8399)	−0.8130[e]
AlI	^{27}Al	−0.7970	(−0.7865)	−0.7852	(−0.7748)	−0.7814	(−0.7714)	−0.7417[c]
GaF	^{69}Ga	−2.6053	(−2.6237)	−2.6846	(−2.6942)	−2.6937	(−2.7112)	−2.76[c]
GaCl	^{69}Ga	−2.2775	(−2.2866)	−2.3462	(−2.3472)	−2.3546	(−2.3627)	−2.38[g]
GaBr	^{69}Ga	−2.1577	(−2.1705)	−2.2131	(−2.2177)	−2.2195	(−2.2312)	−2.24[c]
GaI	^{69}Ga	−2.0507	(−2.0599)	−2.0830	(−2.0846)	−2.0813	(−2.0901)	−2.10[c]
InF	^{115}In	−3.7354	(−3.7418)	−4.0378	(−4.0437)	−4.1338	(−4.1438)	−4.18[c]
InCl	^{115}In	−3.4111	(−3.4140)	−3.6866	(−3.6889)	−3.7787	(−3.7826)	−3.79[c]
InBr	^{115}In	−3.2887	(−3.2966)	−3.5425	(−3.5468)	−3.6296	(−3.6365)	−3.65[c]
InI	^{115}In	−3.1791	(−3.1851)	−3.3956	(−3.3984)	−3.4685	(−3.4749)	−3.49[c]

[a] BP functional and TANH basis for heavy atoms. The EFGs in parentheses and the observed EFGs are from the work of van Lenthe and Baerends.[13] References to the sources of the experimental data are given as additional footnotes. [b] Ref 65. [c] Ref 66. [d] Ref 67. [e] Ref 68. [f] Ref 69. [g] Ref 70.

corrections to the EFG also agree well with the data from ref 13. TlI exhibits a particularly large spin−orbit effect on the iodine EFG (a 23% increase relative to the scalar Z4 value calculated in this work compared to 25% as reported by van Lenthe and Baerends[13]). The Z4 correction terms are largest for the heaviest nucleus among the set of molecules in Table 1, astatine, which is not surprising given the form of the operator $\hat{B}$ in the correction terms. The correction of −3 atomic units is in agreement with the one predicted by Neese et al.[14] As shown by our spin−orbit computations, the spin−orbit effect on the At EFG in HAt is small in comparison, yielding an increase of about 6%. The corresponding spin−orbit coupling induced increase of the iodine EFG in HI is only 2%.

Table 2 lists calculated EFGs at indicated atom centers for a larger set of main group diatomic halides obtained in nonrelativistic (NR), scalar relativistic Z4 (SR-Z4), and spin−orbit Z4 (Z4) computations. The BP functional was used again in order to facilitate a comparison with the literature data (in parentheses[13]). In this table, we also include experimentally observed EFGs for comparison. The values were taken from the work of van Lenthe and Baerends[13] and originally published in the form of measured nuclear quadrupole coupling constants in refs 65−69. The number of significant figures provided for the experimental EFG relates to how accurately the nuclear quadrupole moments are known.[71]

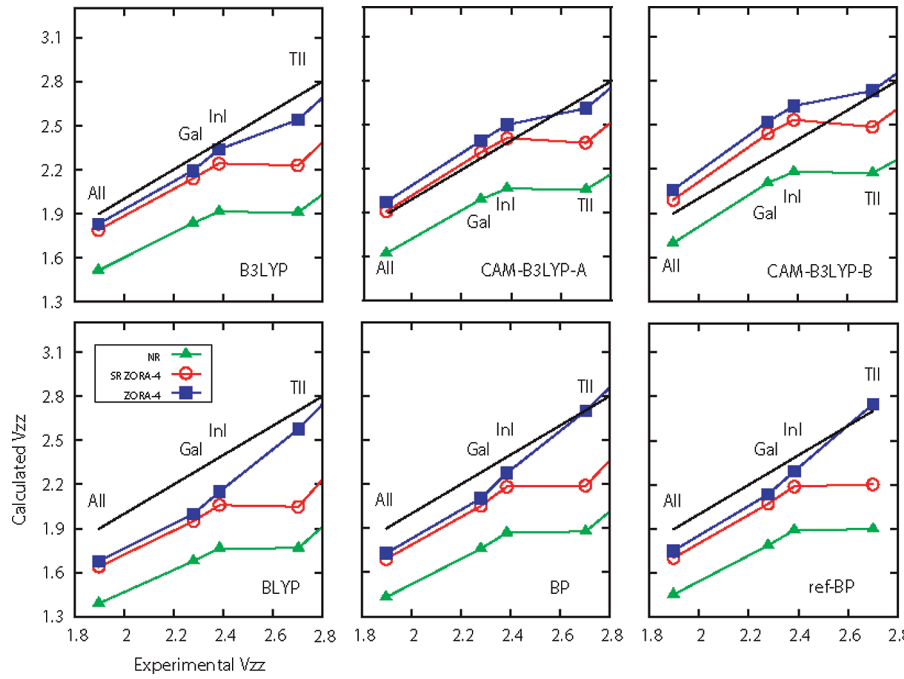

Figure 1. Calculated NR, SR-Z4, and Z4 iodine V_{33} vs experimental values, for different functionals. Atomic units. Straight black lines indicate where calc. = expt. The graph labeled ref-BP shows data from van Lenthe and Baerends[13] for comparison.

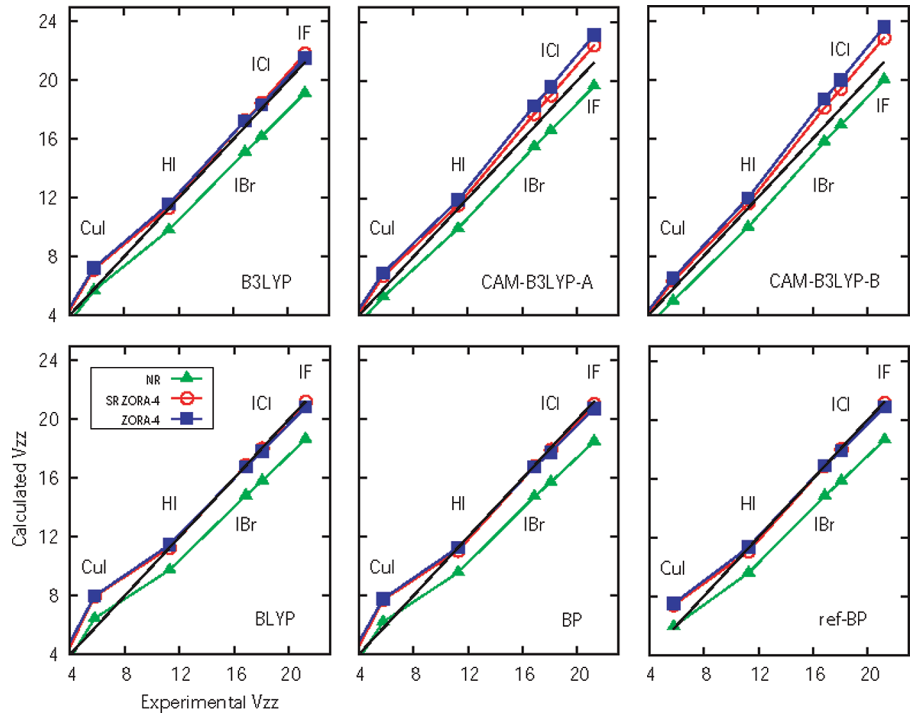

Figure 2. Calculated NR, SR-Z4, and Z4 iodine V_{33} vs experimental values, for different functionals. See also caption of Figure 1.

It is important to keep in mind some of the technical differences between the EFG calculations performed for this work and those from ref 13: van Lenthe and Baerends used Slater-type basis sets, while we used Gaussian-type basis sets. The numerical integration grids are quite different, and the implementations of the ZORA operator differ as well. It is therefore reassuring that Table 2 demonstrates close agreement between our results and those from ref 13 despite the technical differences between the calculations. In Figures 1−4, plots of calculated vs experimental EFGs are shown. We have included calculated data from van Lenthe and Baerends for comparison to demonstrate the close agreement between the different calculations. The agreement with experimental results is generally good, with the exception of the Cu diatomics for which the agreement of the halide EFGs with experimental values is fair. This problem has

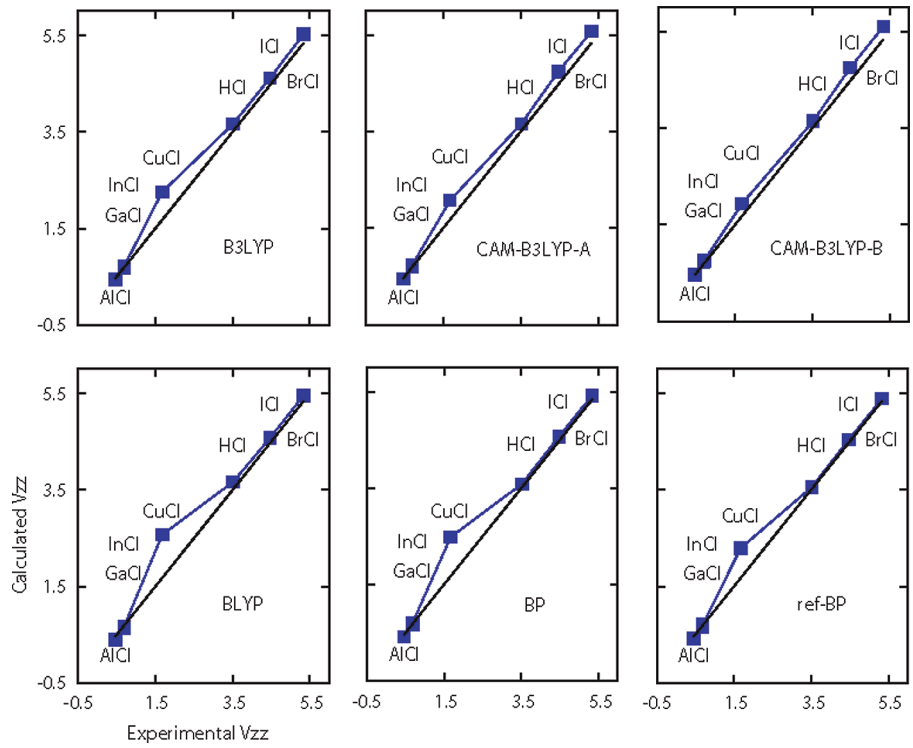

Figure 3. Calculated NR, SR-Z4, and Z4 chlorine V_{33} vs experimental values, for different functionals. See also caption of Figure 1.

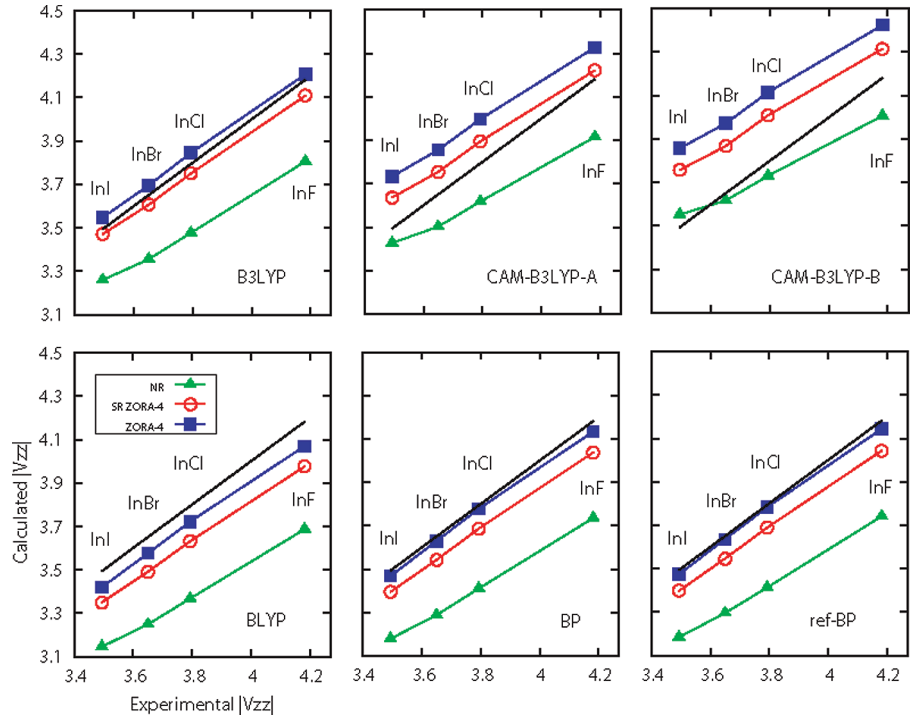

Figure 4. Calculated NR, SR-Z4, and Z4 indium V_{33} (absolute value) vs experimental values, for different functionals. See also caption of Figure 1.

already been noted in ref 13. In these molecules, the Cu EFG calculated with standard functionals even has the wrong sign, a problem that will be discussed in more detail below.

Figures 1−4 also show the dependence of the calculated EFGs when comparing different density functionals. The corresponding numerical data are provided in Tables 11−15 in the Appendix. In addition to BP, the functionals BLYP, B3LYP, and two different parametrizations of CAM-B3LYP are compared for different levels of theory (NR, SR-Z4, and Z4). Figure 1 shows EFGs at iodine for AlI, GaI, InI, and TlI. An important feature of this graph is the behavior of EFG at iodine in TlI, where we observe closer agreement to the experimental value in the following order: NR, SR-Z4, and Z4. This trend holds for all of the functionals studied,

Table 3. Copper and Gold V_{33}, in Atomic Units, Calculated for Selected Diatomics with Z4 and Different Functionals[a]

method[b]	CuH		CuF		CuCl		CuBr		CuI	
BLYP	0.800	(0.776)	0.916	(0.879)	0.731	(0.718)	0.699	(0.696)	0.633	(0.640)
B3LYP	0.486	(0.338)	0.372	(0.112)	0.307	(0.149)	0.312	(0.181)	0.313	(0.208)
CAMB3LYP	0.345	(0.311)	0.190	(0.145)	0.143	(0.129)	0.158	(0.152)	0.173	(0.176)
CAMB3LYP*	−0.048	(−0.085)	−0.461	(−0.503)	−0.303	(−0.315)	−0.231	(−0.237)	−0.146	(−0.141)

method[c]	AuF		AuCl		AuBr		AuI	
BLYP	4.018	(4.005)	3.592	(3.659)	3.485	(3.625)	3.250	(3.445)
B3LYP	2.290	(2.190)	2.208	(2.206)	2.213	(2.280)	2.220	(2.310)
CAMB3LYP	1.571	(1.285)	1.562	(1.384)	1.569	(1.502)	1.639	(1.625)
CAMB3LYP*	−0.512	(−0.858)	−0.058	(−0.290)	0.113	(−0.010)	0.358	(0.332)

[a] The values in parentheses are four-component DFT results from Thierfelder et al.[56] [b] TANH basis set[49] for all atoms except hydrogen where the TZVPP basis set[46] was used. Polarization functions were taken from TZVPP. [c] SARC-ZORA basis set[50] for Au and TANH basis set elsewhere; TZVPP for hydrogen. Polarization functions were taken from TZVPP, except for Au.

and it demonstrates the potential importance of considering spin−orbit relativistic effects in computations of heavy atom EFGs, in particular for heavy p block elements. Relativistic effects are also significant for the indium EFGs (Figure 4) and for the remaining iodine EFGs (Figure 2). For the Cl EFGs of Figure 3, the differences between SR-Z4, Z4, and NR were not very pronounced, and therefore we decided to show only the spin−orbit Z4 data set in the graphs.

Overall, the results for the different sets of molecules show that Z4 is in reasonable agreement with experimental results for all functionals that were considered, unlike the NR calculations. In all cases, our results with the BP functional are very similar to those obtained by van Lenthe and Baerends.[13] As with the data in Table 1, minor differences are most likely due to the different basis sets (GTO vs STO, and the overall number of functions) and numerical integration grids. Good performance of nonhybrid DFT and DFT with standard hybrid functionals for main group atom EFGs has been noted before.[72] Figures 1−4 indicate a slightly better performance of the B3LYP hybrid and the two range-separated CAM-B3LYP parametrizations compared to the nonhybrid functionals BP and BLYP for iodine and chlorine EFGs, whereas for the indium EFGs the results are closest to experimental results with the BP and the B3LYP functionals. For the indium data set, the CAM-B3LYP-B parametrization, which is fully long-range corrected, leads to an overestimation of the EFG magnitudes such that the NR data end up being closer to experimental data—clearly, these are "better" results for the wrong reasons.

4.2. Test Set 2: Copper and Gold Diatomics. Table 3 lists EFG data for Cu and Au in a set of diatomic molecules. The data in parentheses were obtained by Thierfelder et al. with four-component relativistic DFT and very flexible GTO basis sets designed for EFG computations.[56,73] As already mentioned in section 3, we employed the uncontracted TANH basis with polarization functions from TZVPP for Cu and SARC-ZORA for Au. Transition metal EFGs are more challenging to compute than EFGs for main group atoms[72]—at least for diatomic molecules. As the table shows, the dependence of the functional is rather dramatic. The CAM-B3LYP* parametrization yields the desired negative signs for the Cu and Au field gradients in these molecules,[56] while standard nonhybrid and hybrid functionals predict the EFGs with the wrong sign. Given the extreme sensitivity of the EFGs to the functional, the agreement of our results with the four-component DFT data of Thierfelder et al.[56] can be considered good. For example, the deviations of up to 0.3 au between our data and those of ref 56 for the gold EFGs are within 10% of the range of functional dependence for each diatomic. The EFG ranges from AuF to AuI for each functional are also in reasonable agreement with literature data.

Table 4. CuCl: NLMO Analysis of Copper V_{33} (au)[a]

NLMO	B3LYP	CAM	CAM*
σ(Cu−Cl)	−0.443	−0.477	−0.461
$\sum$ 2p	0.058	0.050	0.018
$\sum$ 3p	−0.172	−0.243	−0.461
d_δ (ea.)	8.749	8.750	8.730
d_π (ea.)	−4.308	−4.309	−4.305
d_σ	−7.765	−7.825	−8.005
$\sum$ 3d	1.109	1.057	0.845
$\sum$ analysis	0.552	0.387	−0.059
total calcd	0.295	0.133	−0.304

[a] SRZ4 calculations. CAM = CAM-B3LYP-A, CAM* = CAM-B3LYP*.

The sensitivity of the metal EFGs begs the question, how exactly is V_{33} resulting from a balance between contributions from different orbitals? To address this question, a NLMO analysis as detailed in section 3 has been carried out for the CuCl and CuF diatomics. A careful analysis by Schwerdtfeger et al.[74] of the electron density distribution of CuCl calculated at various levels of theory has previously demonstrated that this system affords a sensitive coupling of the valence and core charge densities which strongly affects calculated properties (EFG, but also the dipole moment). The NLMO data are provided in Tables 4 and 5, with contributions grouped by orbital type. To simplify the interpretation, the analyses were carried out at the SRZ4 level and, for the Cu EFGs, afford results similar to those of spin−orbit Z4. The NBO analysis indicated very little delocalization in both systems; therefore, a separate decomposition of the EFG into contributions from NBOs instead of NLMOs does not offer much additional insight, and we forego a separate discussion of the NBO contributions. In order to assist the discussion, we recall a few details about the role of atomic orbitals for EFGs:[2,75] For a completely ionic bond (Cu^+Cl^-), the EFG vanishes as long as the AOs are not polarized and as long as they completely shield the nuclear charges from the bonding partner. For the EFG component along the bond,

Table 5. CuF: NLMO Analysis of Copper V_{33} (au)[a]

NLMO	B3LYP	CAM	CAM*
σ(Cu−F)	−0.485	−0.508	−0.493
$\sum$ 2p	0.028	0.022	−0.023
$\sum$ 3p	−0.314	−0.388	−0.699
d_δ (ea.)	8.771	8.773	8.738
d_π (ea.)	−4.357	−4.354	−4.342
d_σ	−7.457	−7.547	−7.812
$\sum$ 3d	1.371	1.291	0.980
$\sum$ analysis	0.600	0.417	−0.235
total calcd	0.351	0.173	−0.467

[a] SRZ4 calculations. CAM = CAM-B3LYP-A, CAM* = CAM-B3LYP*.

Table 6. AuCl: NLMO Analysis of Gold V_{33} (au)[a]

NLMO	B3LYP	CAM	CAM*
σ(Au−Cl)	−1.577	−1.702	−1.696
Au core	0.451	0.388	0.136
f_σ	−30.512	−30.510	−30.556
f_π (ea.)	−22.884	−22.882	−22.915
f_δ (ea.)	0.010	0.010	0.010
f_ϕ (ea.)	38.185	38.181	38.234
$\sum$ 4f	0.110	0.108	0.102
5s	−0.028	−0.030	−0.027
$5p_\sigma$	−249.412	−252.528	−250.934
$5p_\pi$ (ea.)	124.512	125.849	124.524
$\sum$ 5p	−0.388	−0.830	−1.886
$5d_\sigma$	−11.370	−11.601	−11.883
$5d_\pi$ (ea.)	−7.513	−7.542	−7.571
$5d_\delta$ (ea.)	15.147	15.213	15.241
$\sum$ 5d	3.898	3.741	3.457
$\sum$ all other NLMOs	−0.135	−0.105	−0.131
$\sum$ analysis	2.331	1.570	−0.045
total calcd	2.332	1.573	−0.040

[a] SRZ4 calculations. CAM = CAM-B3LYP-A, CAM* = CAM-B3LYP*.

V_{33}, with pure atomic orbitals, the d_σ orbital on Cu would contribute a relative increment of −2 to the EFG; the d_π orbitals, −1 each; and the d_δ, increments of +2 each.[2] For a filled atomic d shell, the contributions cancel. For an atomic p shell, the relative magnitudes are −2 for p_σ versus +1 for each p_π. The analysis for CuCl in Table 4 demonstrates that the Cu 3d shell and the 3p semicore shell both contribute significantly to the EFG and that the EFG caused by the Cu 3p and 3d shells accounts for most of the trend going from B3LYP to CAM-B3LYP*.

The d_δ orbitals are nonbonding. Their −8.75 to −8.73 au EFG contribution can therefore be taken as those of pure Cu 3d orbitals. It is reassuring that their EFG contribution remains almost constant between the calculations with the different functionals. For an essentially spherical Cu^+ d^{10} ion, one would then expect approximately 4.37 au from each d_δ and around −8.75 to −8.73 au from the d_σ orbital. The d_π EFG contributions are very close to the idealized value. The minor deviation can be attributed to π interactions between Cu and Cl. However, both for B3LYP and CAM-B3LYP-A, the negative contribution from d_σ is significantly lower than what would be expected for a pure Cu 3d, indicating that with these functionals the d_σ orbital is significantly more involved in the covalent Cu−Cl bond than in the CAM-B3LYP* calculation. The EFG trend for the d_σ reflects the NLMO compositions: For B3LYP, σ(Cu−Cl) has an overall 17% Cu character (the small value reflecting the ionicity of the bond) of which 5.7% is d_σ. For comparison, with CAM-B3LYP*, the bond is somewhat more ionic (12% Cu) but with only a 3.5% admixture of d_σ. The trends for the Cu 4s mixing into the d_σ NLMO go in the same direction: with B3LYP, there is 5.8% Cu 4s in the d_σ NLMO, whereas in the CAM-B3LYP* calculation, the 4s percentage is 3.4%. The effect on the EFG from σ(Cu−Cl) is only minor, but because of the strong EFG caused by even small changes in the occupations and spatial extent of the individual 3d orbitals, the effect on the EFG contribution from d_σ is large. The EFG contributions from the Cu 3p shell can be attributed to electrostatic polarization by the nonspherical environment and valence-core orthogonalization.

The CuF data in Table 5 show that this case is very similar to CuCl, except the bond is more ionic, as indicated by a smaller percentage of Cu orbitals in the σ(Cu−F) NLMOs (ranging from 10.9% with B3LYP to 6.8% with CAM-B3LYP*) compared to CuCl. We should point out that a breakdown of the EFG in CuF in terms of orbital contributions has also been given in ref 25, where the authors stated that the "total EFG for the Cu 3d shell adds up to 8.1, 13.3, and 12.3 au at the HF, LDA and B3LYP level of theory", which was found to be balanced by contributions from fluorine 2p. The EFG and its functional dependence were mainly attributed to polarization of the Cu 3d shell. From our analyses on CuF and CuCl, we find that the contributions from the Cu 3d shell are definitely crucial, but it appears that hybridization, i.e., the extent of how much the Cu $3d_\sigma$ participates in the bonding and how well the polarization of the 3p shell is described, are major factors deciding which functional performs best. It is known that for Cu(II) systems calculated with standard functionals the metal d shell binds too strongly covalently.[76] Although the Cu−X diatomics are very different systems, a similar problem might be manifesting here in the form of a too strong involvement of the Cu $3d_\sigma$ orbital in the Cu−X bond.

For comparison, and to investigate relative contributions to the EFG from f orbitals, a NLMO decomposition was also carried out for the Au EFG in AuCl. The SRZ4 data are collected in Table 6. Regarding the sign and relative magnitude of EFG contributions from idealized atomic f shells (spin-free), see Figure 5. The f_δ orbitals have cubically symmetric charge densities and therefore do not contribute to the EFG at their atomic center. The calculated EFG contributions for the gold 4f shell listed in Table 6 nicely follow the ratios predicted from the simple AO model. For instance, the negative $4f_\sigma$ contribution ($V_{33} = V_{zz}$) is 1.333 times those from each $4f_\pi$ (idealized AOs: 4/3). The $4f_\delta$ contributions are effectively zero (the small EFG indicating a slight polarization of the 4f shell along with nonspherically symmetric valence-core polarization effects), and the ratio of the $4f_\phi$ to the $4f_\pi$ EFG terms of 1.669 for AuCl is also in excellent agreement with the idealized value of −5/3 from Figure 5. Overall, the 4f shell is not a dominant source of the EFG in AuCl when calculated with the B3LYP and CAM-B3LYP functionals. For CAM-B3LYP*, the calculated net EFG almost vanishes as a result of a cancellation of terms with opposite signs. The origin of the rather large EFGs calculated with B3LYP and CAM-B3LYP is seen to be similar to that for CuCl. A closer inspection of the NLMO

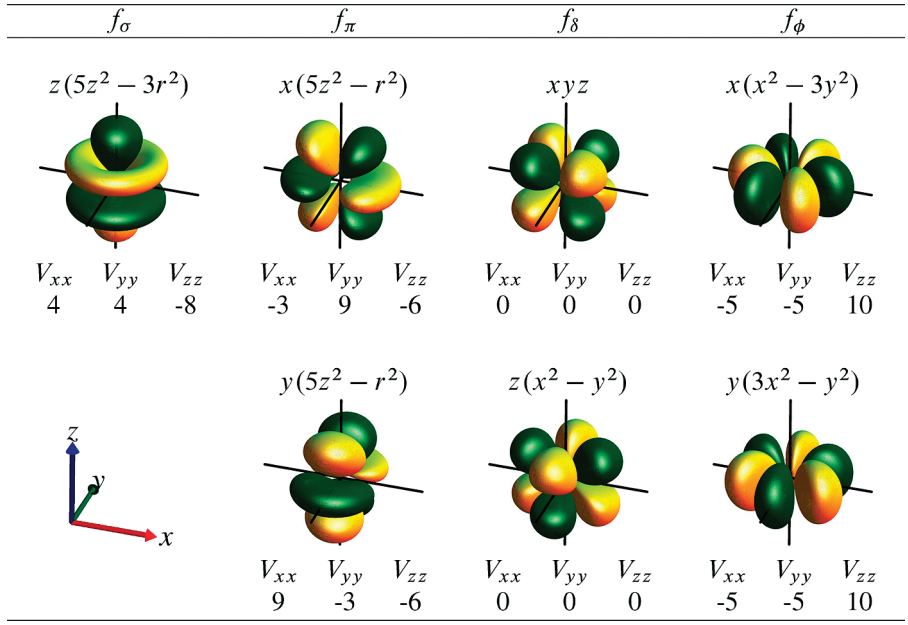

Figure 5. Sign and relative magnitude of EFG contributions from atomic f shells (spin-free), calculated analytically from 4f orbitals $N\Omega(x, y, z)\ e^{-\alpha r}$ and the nonrelativistic EFG operator, with Ω as indicated in the figures and *N* being a normalization constant. The EFG values listed are in units of $2\alpha^3/630$ per double occupation. Symmetry labels with respect to *z* axis.

compositions also showed that the trends going from B3LYP to CAM-B3LYP* are similar, with the bond becoming slightly more ionic, the d character in the bond NLMO decreasing, and the s character of the $5d_\sigma$ NLMO decreasing. The net positive EFG from 5d remains substantial, however. Core polarization (1s to 4d) and valence-core orthogonalization also play a role, as seen from the combined Au core terms in Table 6. As we have argued elsewhere,[2] in accord with other researchers,[48,74] the core terms are coupled to the valence EFG terms. For AuCl, they follow in sign the overall trend seen for the functionals, i.e., the EFG becoming less positive when going from B3LYP to CAM-B3LYP*. The 5p semicore orbitals have very large EFG contributions individually, indicating that even a slight imbalance among these orbitals with respect to a spherically symmetric p shell can cause a sizable EFG. The combined 5p EFG contributions in AuCl follow the same trend as 5d and the core terms, becoming more negative when going from B3LYP to CAM-B3LYP*, and provide the largest individual fraction of the overall trend.

4.3. Ru and Nb Complexes. The present section focuses on metal EFGs in Ru and Nb complexes. Each of these complexes exhibits a particular, different role of the valence d shell population for the EFG, as analyzed recently.[2] There are also numerous important applications of complexes of this type, as well as fundamental interest from a structure and bonding viewpoint. For instance, the complex $[RuCl_4N]^-$ features a formal Ru−nitrogen triple bond and an unusual oxidation state. Ruthenocene, $Ru(C_5H_5)_2$, has long fascinated chemists. Among its applications, it has the ability to transfer electrons, which makes it a good photoinitiator for polymerization reactions.[77] There are numerous papers on $[Ru(bipy_3)]^{2+}$ and its derivatives, and similar complexes with bidentate unsaturated ligands, with proposed applications in fields as diverse as photovoltaics,[78,79] materials science,[80−83] biology,[84] biochemistry,[85] and medicine.[85−89] The half-sandwich niobium metallocenes $CpNbCl_4$ and $CpNb(CO)_4$ are interesting, for instance, because of their applications in catalysis.[90]

Table 7. Computed Ru V_{33}, in Atomic Units, for $[RuCl_4N]^-$ Using Different Levels of Theory[a]

	CAM-B3LYP-A	B3LYP	revPBE
ZORA/6-311G**	4.776	4.416	4.033
Z4/6-311G**	4.693	4.346	3.969
Z4/6-31G*	4.691	4.347	3.972
ZORA/ANO-(H set)	4.766	4.422	4.031
Z4/ANO-(H set)	4.683	4.350	3.968
ZORA/ANO-(G,H set)	4.806	4.455	4.052
Z4/ANO-(G,H set)	4.724	4.383	3.989

[a] ANO-(G,H set) is ANO-RCC for Ru but with *h* or *g*, *h* functions removed from the basis. See text for details.

We first investigate the basis set dependence of the metal EFGs. The ANO basis set used for the metal in these calculations contains functions with a high angular momentum that may serve as polarization functions but is also important in correlated wave function electronic structure methods to describe correlation. In DFT calculations, one might be able to exclude the *h* set and perhaps even the *g* set. There is also the question of how flexible the ligand basis set has to be. Table 7 provides calculated ruthenium EFGs in $[RuCl_4N]^-$ at the ZORA spin−orbit level, with and without Z4 corrections, for several functionals with the following basis sets: ANO for Ru and 6-31G* versus 6-311G** for the ligand atoms and ANO versus ANO-(H set) versus ANO-(G,H sets) along with 6-31G* to study the effect of removing *g* and *h* functions from the metal basis. From these calculations, we observe the following: (i) The effect of adding the Z4 corrections lowers the EFG values by about 2% for all the functionals tested. (ii) Using a more flexible basis set than 6-31G* for the ligands does not affect the EFG at Ru noticeably. This allows a significant reduction of the computational cost for larger systems. (iii) Removing

Table 8. Computed Spin−Orbit Z4 and Experimental Metal Atom V_{33}, in Atomic Units, for Selected Ru and Nb Complexes[a]

	CAM-B3LYP-A	B3LYP	revPBE	|expt|[b]
$[RuCl_4N]^-$	4.691	4.347 (4.33)	3.972 (3.94)	4.27(16)
$Ru(C_5H_5)_2$	1.917	1.659 (1.98)	1.377 (1.66)	1.15(5)
$[Ru(bipy_3)]^{2+}$	−0.190	−0.283 (−0.23)	−0.378 (−0.36)	<0.21
$CpNbCl_4$	1.406	1.312 (1.28)	1.278 (1.26)	0.72(5)
$CpNbCl_4$ [c]	1.394	1.297	1.262	
$CpNb(CO)_4$	0.225	0.240 (0.24)	0.274 (0.27)	0.01(0)
$CpNb(CO)_4$[c]	0.238	0.253	0.292	

[a] The calculated EFGs in parentheses were taken from ref 2. [b] Experimental EFGs for ruthenium complexes were calculated in ref 91 from Mössbauer quadrupole splittings reported in ref 92. Experimental EFGs for the niobium complexes were calculated from the solid-state ^{93}Nb NMR quadrupole coupling constant of ref 93 using a nuclear quadrupole moment of −0.320(20) barn.[71] [c] Using uncontracted TANH basis set for niobium.

the *h* functions from the ANO basis for Ru has a negligible effect. When removing both the *g* and *h* sets, the EFG at Ru varies by less than 1% compared to the full ANO basis. Thus, it appears that in DFT computations of EFGs for the 4d metals, the high-angular momentum basis functions in the ANO basis are of little benefit. This is most likely due to the fact that electron correlation in DFT is obtained from the integration of a rather smooth electron density and its derivatives in the exchange-correlation functional, while in correlated wave function methods, high angular momentum basis functions are required for better approximating the electron cusps in the wave function.

Table 8 lists Z4 EFG data calculated for a set of ruthenium and niobium complexes using the CAM-B3LYP-A, B3LYP, and revPBE functionals. The calculated EFGs in parentheses were taken from ref 2 where SR-Z4 was used along with a Slater-type TZ2P basis set and optimized geometries. We employed the same optimized geometries for easier comparison. The technical differences between the EFG implementations are the same as those for the comparison of main group diatomics in Table 2, apart from the spin−orbit corrections which were consistently used in the present work. There is overall good agreement with the reference data of ref 2, indicating that spin−orbit relativistic contributions to the Nb and Ru EFGs are not very important. However, the calculations for this work were carried out at the spin−orbit level to demonstrate that routine calculations of this type can be performed for these and other metal complexes and organometallic systems. For comparison, we have also carried out calculations on the Nb complexes with the TANH basis, which yields very similar results. The differences from the ANO basis are smaller than 0.02 au in magnitude, which is significantly smaller than the variations among the different functionals.

The origin of a nonzero EFG in the Ru complexes has been analyzed recently:[2] For $[Ru\ (bipy_3)]^{2+}$, the origin of the relatively small field gradient is a compression of the pseudo-octahedral nitrogen arrangement along the 3-fold symmetry axis of the complex, causing less involvement of the Ru $4d_{z^2}$ orbital in metal−ligand π backbonding than for the other two occupied Ru 4d orbitals (negative V_{33} contributions), which is only partially counterbalanced by positive V_{33} contributions from Ru−N σ bonding orbitals created by the structural distortion. In ruthenocene, the EFG is caused by a strongly nonspherical charge distribution in the 4d shell due to the formal $(4d_{xy})^2(4d_{x^2-y^2})^2(4d_{z^2})^2$ configuration, which is to some extent balanced by significant π donation from Cp to the metal and by δ backbonding from the metal. In $[RuCl_4N]^-$, the large EFG is mainly caused by the double occupation of just one 4d orbital, creating a strongly nonspherical electronic charge density in the Ru 4d shell.

The calculations performed here with different density functionals show a modest dependence of the EFGs on the description of exchange and correlation, with a trend of more positive Ru EFG along the series revPBE, B3LYP, and CAM-B3LYP. This trend leads to slightly better agreement with experimentally derived EFGs for the tris-bipyridyl complex with CAM-B3LYP, but for $[RuCl_4N]^-$ the EFG calculated with CAM-B3LYP appears to be somewhat overestimated. Overall, however, the functional dependence is not as pronounced as those for the transition metal diatomics of the previous section. For instance, unlike for the case of Au and Cu, the differences between functionals are much smaller than the range of EFGs spanned by the set of complexes (which, of course, depends on the selection of the test set). The performance of all functionals and the combination of basis sets used here with Z4 therefore appears to be suitable for routine calculations on these larger metal complexes to rationalize and analyze EFG trends among them.

The gas-phase calculated EFGs in the Nb complexes show greater discrepancy with experimental values than the Ru EFGs, likely because the experimental results are derived from solid-state NMR measurements, while longer range effects on the EFG from the crystal environment and effects from nearest neighbor contacts are not included in the calculations. The origin of the EFGs in the Nb complexes can be traced back to a complex interplay of metal−ligand bonding and backbonding involving the Nb 4d shell, which is sensitive to the computational model used to describe the environment of the complexes. As for the Ru complexes, the EFGs calculated for this work are in good agreement with the SR-Z4 STO basis set data from ref 2, and the level of theory appears to be well suited for routine calculations at the two-component relativistic DFT level of theory.

4.4. Uranyl Salts. Uranyl, UO_2^{2+}, ions are important benchmark systems for actinide electronic structure calculations due to their size, symmetric geometry, closed shell nature, chemical stability, and prescence in plenty of compounds. As deceptively simple that uranyl might appear, it challenges quantum mechanical approaches by requiring high level electron−electron correlation methods, flexible basis sets, and—of course—relativistic methods (preferably including spin−orbit coupling).[94−96] Since the EFG is a

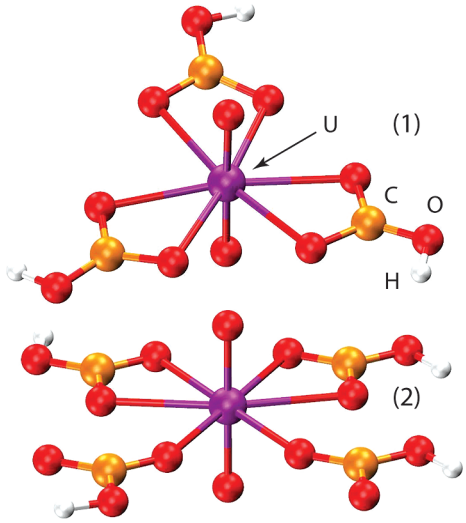

Figure 6. Geometries of uranium complexes. **1** has a U−O bond length of 1.791 Å and a O−U−O bond angle of 179.0°. **2** has a U−O bond length of 1.743 Å and a O−U−O bond angle of 178.6°.

Table 9. Computed Uranium V_{33}, in Atomic Units, in Uranyl and Uranyl Complexes.[a] Spin−Orbit Z4 Computations

	CAM-B3LYP-A	B3LYP	revPBE	BP
$[UO_2(HCO_3)_3]^-$ (**1**)[c]	9.02	7.36	5.76	
$[UO_2]^{2+}$ of (**1**)	−7.99	−9.46	−10.96	
$[UO_2(HCO_3)_4]^{2-}$ (**2**)[c]	11.19	9.40	7.66	
$[UO_2]^{2+}$ of (**2**)	−5.12	−6.67	−8.36	−8.88
$[UO_2]^{2+}$ of (**2**)[b]	−5.32	−6.86	−8.58	−9.12
$[UO_2]^{2+}$ (**3**)				−11.08 (−10.58)

[a] Using the ANO-RCC basis set for uranium and TZVPP for oxygens and using Cartesian (6d, 10f, 15 g) angular functions unless explicitly stated otherwise. [b] Using the ANO-RCC basis for U and O. [c] Using spherical (5d,7f,9g) angular functions.

sensitive indicator of the ground state electronic structure around a metal, it serves as a particularly suitable "probe" for comparing different density functionals. A broader interest in studying uranium and other actinide compounds arises from the nuclear waste problem. In particular, carbonate complexes have been identified as important uranyl species in natural waters.[97]

Figure 6 shows the geometries of two uranyl carbonate complexes considered here for calculations of uranium EFGs. The geometries were taken from X-ray crystalline structures of two uranyl salts:[95] $(NH_4)_4UO_2(CO_3)_3$ (**1**) and rutherfordine ($UO_2(CO_3)$; **2**). In these salts, the uranyl moiety has different coordinations by the carbonate ligands. In some calculations, protons were added to the clusters cut from the crystal structures, changing CO_3^{2-} to HCO_3^-, in order to reduce the overall charges. For comparison with ref 48, we included in our study a third geometry labeled **3**, which is a perfectly linear UO_2 molecule having a U−O bond lengh of 1.78 Å. In Table 9, the uranium EFGs are collected for complexes **1** and **2**, calculated with the CAM-B3LYP-A, B3LYP, and revPBE functionals. Additional EFG calculations were performed on the corresponding uranyl moiety in **1** and **2** using OUO bond angles and U−O bond lengths as adopted in geometries **1** and **2**, respectively.

From the results shown in the table, we observe a change in sign in the EFG at U upon complexation with carbonate, from negative in free uranyl and for the isolated uranyl moieties of **1** and **2** to positive in the presence of equatorial ligands. Such a behavior of the uranium EFGs due to ligand coordination has been discussed in previous works by Belanzoni et al. and de Jong et al.[48,98] and has been studied for different coordinations. Table 9 also lists the EFG at U for geometry **3** calculated with the BP functional. This value is in very good agreement with the EFG shown in parentheses which was taken from Belanzoni et al.[48] (STO basis sets, same geometry). The table also demonstrates the effect of using different sized basis sets for the uranyl oxygens: TZVPP (11s,6p,2d,1f) versus an uncontracted ANO-RCC basis (14s,9p,4d,3f). We observe that the EFG at uranium is increased by about 0.2 au with the larger basis set with the different functionals. Compared to the more than 3 au variation among the functionals, this basis set effect is not particularly significant, and the more economic TZVPP basis can be used in calculations of the metal EFG. Additional SR-Z4 calculations discussed below indicated that even with the relatively small 6-31G* basis for O, the uranium EFG does not change significantly. The magnitudes of the EFGs at U in the free uranyl ion for the four exchange-correlation functionals tend to decrease in the order shown in the table from right to left, i.e., when going from nonhybrid to a standard hybrid to the Coulomb-attenuated hybrid. The trend for the complexated uranyl ions **1** and **2** goes in the same direction of less negative EFG, thereby increasing the magnitude of the positive EFG from BP and revPBE to CAM-B3LYP. Experimental EFGs have to our knowledge not been determined for the carbonate complexes. However, for the related nitrate complexes investigated by Belanzoni et al., the experimental estimate derived from Mössbauer data is $+8.38 \pm 0.13$ au,[99] which is in reasonable agreement with our data.

It is interesting to dissect the uranyl EFG and the sign change upon complexation in the equatorial plane with the localized orbital EFG analysis. To this end, we have performed such calculations at the SR-Z4 level of theory, similar to those for Cu and Au of section 4.2. A thorough analysis of the uranyl EFG based on MOs and AOs has been carried out by Belanzoni et al.,[48] which therefore allows comparisons with the results from the previous analysis. See also de Jong et al.[98] Of particular interest are the AO contributions from the U 6p, 6d, and 5f. It was pointed out by Pyykkö that the positive EFG in the experimentally observed systems might be a signature of a 6p hole.[100,101] Belanzoni et al. confirmed the presence of a partial 6p hole, but as in our study, the net EFG in free uranyl was found to be negative in part due to a nonspherical electron distribution in the valence 5f shell from the bonding of uranium to the oxygens. Only in the systems with equatorial ligands is a positive EFG computed.

The relative magnitudes of EFG contributions from atomic shells were already discussed in section 4.2 (see also ref 2). For holes in otherwise filled atomic shells, the "contributions" (i.e., lack of electronic EFG) have the opposite sign. For uranyl oriented along the z axis, V_{33} is equal to V_{zz}. The f

orbitals in Figure 5 are then conveniently grouped into a single f_σ, two f_π, two f_δ, and two f_ϕ. The f_δ's do not contribute to the EFG. On the basis of their computational analysis, Belanzoni et al. assigned to free UO_2^{2+} an approximate effective electron configuration of $6s^26p^65f_\sigma^15f_\pi^26d_\pi^17s^2$ for U. The effective atomic population can be considered formally as arising from the U(VI) f^0 ion binding to two O^{2-}'s. From Figure 5, it is seen that the EFG from the 5f occupations would be cumulative since f_σ and f_π contribute with negative signs to V_{zz}. Partial d_π occupations would cause a negative V_{33} as well, while spherical 6s, 7s, and the filled 6p shells would not be expected to give rise to a field gradient at the U nucleus. The main source of the large negative EFG in free UO_2^{2+} would then be from the nonspherical 5f charge density. Upon coordination by ligands in the equatorial plane, the formally empty f_ϕ orbitals become suitable electronic charge acceptors (see Figure 5). The potentially large positive V_{33} contributions from these and partially occupied equatorial $6d_\delta$ orbitals on uranium were identified in ref 48 as a major source for the EFG sign change. However, it was also noted that it was "difficult to interpret the total EFG quantitatively in terms of a simple chemical bonding picture", because of canceling terms that individually far exceeded the magnitude of the net EFG.

When considering the effective uranium atomic configuration as devised by Belanzoni et al., relative to U(VI) there are six excess electrons at U, so the bonding pattern might be considered as $[O{\equiv}U{\equiv}O]^{2+}$. This is in fact the calculated bonding pattern assigned from the NBO analysis based on the calculated scalar ZORA density matrix, along with an assignment of $5f^{2.50}6s^26p^26d^{0.45}7s^{0.06}$ for the uranium valence configuration, based on its natural atomic orbital populations. The d and f occupations are quite consistent with the effective populations deduced by Belanzoni et al. A low occupation of one of each of the U−O bonding NBOs (1.86 for each σ bond NBO) indicates that these are not to be interpreted as simple textbook covalent bonds but partially as delocalized lone pairs.

The EFG data for the analysis are collected in Table 10. The sign change upon complexation in the equatorial plane is obtained also at the scalar relativistic level. A comparison with the spin−orbit data of Table 9 indicates fairly pronounced spin−orbit effects, but for semiquantitative purposes, scalar relativistic calculations are certainly suitable. The analysis data were obtained with the 6-31G* basis for the ligand atoms instead of TZVPP because of difficulties that the NBO procedure had assigning the bonding patterns in complex **1** when using the larger ligand basis. For comparison, the SR-Z4 EFG in uranyl calculated with TZVPP for the oxygens is −7.422 and is seen to be very close to the value listed in Table 10. According to the NLMO decomposition of the field gradient in UO_2^{2+}, the U−O bonds are the source of a large negative EFG. A breakdown of the σ and π bonding NLMOs shows virtually no U p character and a strong dominance of f_σ in the σ bonds, along with about 78% uranium f_π and 20% d_π at U for the π bonding NLMOs. Because of the nature of the participating U orbitals, donation of electronic charge from the oxygens into f_σ, f_π, d_σ, and d_π naturally yields a negative EFG from the U−O bonds. The second largest influence on the EFG comes from the formally filled 6sp semicore shell. The 6p contribution is indeed positive, as anticipated, and partially balanced by a significant negative contribution from U "6s" (which is obviously not perfectly spherically symmetric). The cumulative U core (1s through 5d) contributions to the EFG are also negative. Somewhat unintuitive are additional sizable negative contributions from the oxygen σ lone pair NLMOs. However, the NLMO breakdown in Table 10 indicates that there is some delocalization of these orbitals in UO_2^{2+}, with participation of U 7s and $5f_\sigma$, with the resulting partial occupation of the latter again giving rise to a negative EFG. One should also keep in mind that the NLMO decomposition includes electronic and nuclear terms, that is, EFG contributions related to how well or not a particular orbital shields the charge from a neighboring nucleus. The localized orbital decomposition of the uranyl EFG is therefore seen to be rather straightforward, it yields a compact analysis, and overall it supports the conclusions drawn by Belanzoni et al.[48]

Table 10. NLMO Analysis of V_{33} (au) at Uranium in the UO_2^{2+} Moiety of **1** and the Uranyl Salt (**1**)[a]

NLMO	$[UO_2]^{2+}$	**1**
σ(U−O)[b] (ea., × 2)	−2.641	−2.372
π(U−O)[c] (ea., × 4)	−0.710	−0.432
eq. U−O bonds		2.529
Σ U−O bonding	−8.122	−3.943
O core ax.	−0.176	−0.202
O LP[d] ax.	−2.684	−2.226
Σ O-eq LP		0.092
U core [e]	−1.239	1.747
U 6s	−1.272	−0.945
U $6p_\sigma$	−66.830	−104.239
U $6p_\pi$ (ea.)	36.459	57.945
Σ U 6s, 6p	4.815	10.706
O core eq.		0.154
Σ other NLMOs		0.485
total calcd	−7.406	6.815

[a] SRZ4, B3LYP. See text for details. [b] σ(U−O) (av.): 30.4% U [s (2.7%), p (0.2%), d (8.5%), f (88.6%)], 67.4% O_α [s (6.4%), p (93.2%), d (0.4%), f (0.0%)], 2.2% O_β [s (11.8%), p (88.0%), d (0.2%), f (0.0%)]. [c] π(U−O) (av.): 20.5% U [s (0.0%), p (0.3%), d (20.1%), f (78.3%), g (1.4%)], 78.9% O_α [s (0.0%), p (99.7%), d (0.3%), f (0.0%), g (0.0%)], 0.7% O_β [s (0.1%), p (96.0%), d (3.9%), f (0.0%), g (0.0%)]. [d] O LP (ea.): 0.6% U [s (83.1%), p (1.4%), d (2.3%), f (12.8%), g (0.5%)], 99.4% O_α [s (93.5%), p (6.5%), d (0.0%), f (0.0%), g (0.0%)]. [e] Core orbitals: 1s−5d.

For the carbonate complex **1**, the juxtaposition of the analysis data with those for UO_2^{2+} reveals several trends. The equatorial U−O interactions show up directly in the form of positive contributions to the U EFG, consistent with an involvement of $6p_\delta$ and $5f_\phi$ (see also Figure 5). Further, the electron density rearrangement caused by the presence of the equatorial ligands leads to a reduced EFG from the axial U−O bonds (both σ and π) relative to free UO_2^{2+}, to a sign change of the U core EFG, and to a significantly increased positive EFG from the uranium 6p shell. The almost 11 au EFG contributions from the 6p shell now represent the largest individual influence on the EFG. Closer inspection of the NBOs revealed an occupation of only 1.78 for $6p_\sigma$ in

complex **1**, which very clearly indicates a partial $6p_\sigma$ "hole" and rationalizes the overall positive EFG in the complex. The corresponding NLMO has almost 5% contribution from the axial oxygens. For comparison, the $6p_\pi$ NBOs have occupations greater than 1.99.

5. Concluding Remarks and Outlook

The new implementation of the Z4 and SR-Z4 approaches for calculations of nuclear EFGs in molecules has demonstrated good agreement with published benchmark data where available, and with experimental results. For the main group diatomics previously studied by van Lenthe and Baerends with a nonhybrid Z4 method,[13] a comparison of different functionals including a range-separated hybrid has shown that the EFGs are quite robust with respect to the choice of functional. Modest improvements are obtained with the hybrid functionals. For transition metals, we were able to confirm the strong dependence on the functional in Cu and Au diatomic molecules, but for larger transition metal complexes the results did not vary so dramatically. Relativistic effects for heavy nucleus EFGs are highly important, with the scalar relativistic effects on the two-component density providing the largest effect. The Z4 correction was in many cases of similar magnitude as effects on the EFG due to spin−orbit coupling. Both should be considered for accurate computations. The basis set combinations used in this work allow for comparatively fast routine EFG calculations. With DFT, the high angular momentum functions in the ANO basis sets appear to be of little benefit in EFG computations on transition metal systems. A localized MO analysis was implemented to assist chemically intuitive interpretations of the results. For CuF, CuCl, AuCl, and the uranyl systems, the localized orbital decomposition has clearly shown the role of individual valence metal p, d, and f shells; bonding and nonbonding orbitals; and core orbitals. The NLMO decomposition leads to rather compact analyses. For f orbitals, a Townes-Dailey like AO model has been set up. The calculations on AuCl showed that for a relatively unperturbed f core shell the EFG signs and magnitudes of the f_σ, f_π, f_δ, and f_ϕ orbitals almost exactly match the model. For uranyl, the analysis demonstrated the delicate balance between EFG contributions from the various semicore and valence orbitals, leading to conclusions that agree well with those drawn by Belanzoni et al.[48]

Acknowledgment. The authors acknowledge support of this research from the Center of Computational Research at SUNY Buffalo, and financial support from the US Department of Energy, grant no. DE-SC0001136 (BES Heavy Element Chemistry Program). Some calculations were performed using EMSL, a national scientific user facility sponsored by the Department of Energy's Office of Biological and Environmental Research and located at Pacific Northwest National Laboratory. N.G. would like to acknowledge the DOE BES Heavy Element Chemistry Program (PI: De Jong) of the U.S. Department of Energy, Office of Science for helping support the ZORA code development.

Appendix

For completeness, numerical data for diatomics calculated with different functionals are provided in Tables 11−15).

Table 11. Calculated Electric Field Gradient, V_{33}, at the Halide Nucleus for a Set of Diatomics, Using the BLYP Functional

		NR	SR-Z4	Z4	observed
AlCl	^{35}Cl	0.3994	0.4028	0.4030	0.4602[a]
GaCl	^{35}Cl	0.6233	0.6312	0.6330	0.6880[b]
InCl	^{35}Cl	0.6407	0.6603	0.6724	0.6933[b]
CuCl	^{35}Cl	2.3592	2.5695	2.5698	1.675[a]
HCl	^{35}Cl	3.6209	3.6657	3.6661	3.516[c]
ICl	^{35}Cl	4.6109	4.6972	4.5785	4.472[c]
BrCl	^{35}Cl	5.4136	5.4758	5.4553	5.336[c]
AlBr	^{79}Br	0.9096	0.9734	0.9773	1.112[d]
GaBr	^{79}Br	1.2458	1.3254	1.3344	1.50[b]
InBr	^{79}Br	1.2954	1.3940	1.4274	1.57[b]
CuBr	^{79}Br	4.6492	5.3150	5.3196	3.71[e]
HBr	^{79}Br	7.1944	7.6538	7.6804	7.55[c]
IBr	^{79}Br	9.3754	9.9780	9.8329	9.89[b]
BrCl	^{79}Br	11.6868	12.3605	12.3422	12.4[c]
AlI	^{127}I	1.3886	1.6377	1.6754	1.90[b]
GaI	^{127}I	1.6771	1.9495	1.9984	2.28[b]
InI	^{127}I	1.7646	2.0604	2.1479	2.38[b]
TlI	^{127}I	1.7660	2.0472	2.5754	2.70[b]
CuI	^{127}I	6.4486	7.9596	7.9937	5.79[e]
HI	^{127}I	9.7557	11.2543	11.4814	11.3[c]
IBr	^{127}I	14.8109	16.8499	16.7877	16.8[c]
ICl	^{127}I	15.8279	18.0085	17.8228	18.1[c]
IF	^{127}I	18.6571	21.1839	20.8508	21.2[c]
AlF	^{27}Al	−1.1388	−1.1432	−1.1433	−1.096[b]
AlCl	^{27}Al	−0.9400	−0.9420	−0.9421	−0.8828[b]
AlBr	^{27}Al	−0.8738	−0.8699	−0.8692	−0.8130[d]
AlI	^{27}Al	−0.8165	−0.8038	−0.7997	−0.7417[b]
GaF	^{69}Ga	−2.5865	−2.6624	−2.6714	−2.76[b]
GaCl	^{69}Ga	−2.2630	−2.3287	−2.3371	−2.38[f]
GaBr	^{69}Ga	−2.1457	−2.1981	−2.2043	−2.24[b]
GaI	^{69}Ga	−2.0441	−2.0729	−2.0702	−2.10[b]
InF	^{115}In	−3.6863	−3.9757	−4.0698	−4.18[b]
InCl	^{115}In	−3.3674	−3.6310	−3.7216	−3.79[b]
InBr	^{115}In	−3.2481	−3.4905	−3.5759	−3.65[b]
InI	^{115}In	−3.1454	−3.3500	−3.4157	−3.49[b]

[a] Ref 65. [b] Ref 66. [c] Ref 67. [d] Ref 68. [e] Ref 69. [f] Ref 70.

Table 12. Calculated Electric Field Gradient, V_{33}, at the Halide Nucleus for a Set of Diatomics, Using the the B3LYP Functional

		NR	SR-Z4	Z4	observed
AlCl	^{35}Cl	0.4387	0.4425	0.4426	0.4602[a]
GaCl	^{35}Cl	0.6727	0.6815	0.6834	0.6880[b]
InCl	^{35}Cl	0.6867	0.7083	0.7201	0.6933[b]
CuCl	^{35}Cl	2.0518	2.2554	2.2558	1.675[a]
HCl	^{35}Cl	3.6204	3.6655	3.6660	3.516[c]
ICl	^{35}Cl	4.6494	4.7359	4.6182	4.472[c]
BrCl	^{35}Cl	5.4777	5.5405	5.5204	5.336[c]
AlBr	^{79}Br	0.9873	1.0571	1.0614	1.112[d]
GaBr	^{79}Br	1.3459	1.4339	1.4434	1.50[b]
InBr	^{79}Br	1.3894	1.4988	1.5318	1.57[b]
CuBr	^{79}Br	4.0692	4.7062	4.7176	3.71[e]
HBr	^{79}Br	7.1945	7.6624	7.6899	7.55[c]
IBr	^{79}Br	9.4886	10.1104	9.9667	9.89[b]
BrCl	^{79}Br	11.8773	12.5782	12.5671	12.4[c]
AlI	^{127}I	1.5135	1.7884	1.8303	1.90[b]
GaI	^{127}I	1.8355	2.1397	2.1934	2.28[b]
InI	^{127}I	1.9136	2.2425	2.3387	2.38[b]
TlI	^{127}I	1.9085	2.2287	2.5395	2.70[b]
CuI	^{127}I	5.6985	7.1362	7.2312	5.79[e]
HI	^{127}I	9.8002	11.3443	11.5819	11.3[c]

Table 12. Continued

		NR	SR-Z4	Z4	observed
IBr	^{127}I	15.1145	17.2600	17.2468	16.8[c]
ICl	^{127}I	16.1665	18.4638	18.3318	18.1[c]
IF	^{127}I	19.1211	21.7892	21.5091	21.2[c]
AlF	^{27}Al	−1.1600	−1.1646	−1.1646	−1.096[b]
AlCl	^{27}Al	−0.9576	−0.9597	−0.9597	−0.8828[b]
AlBr	^{27}Al	−0.8909	−0.8868	−0.8862	−0.8130[d]
AlI	^{27}Al	−0.8341	−0.8207	−0.8171	−0.7417[b]
GaF	^{69}Ga	−2.6583	−2.7370	−2.7464	−2.76[b]
GaCl	^{69}Ga	−2.3211	−2.3882	−2.3968	−2.38[f]
GaBr	^{69}Ga	−2.2002	−2.2524	−2.2589	−2.24[b]
GaI	^{69}Ga	−2.1007	−2.1282	−2.1269	−2.10[b]
InF	^{115}In	−3.8055	−4.1081	−4.2062	−4.18[b]
InCl	^{115}In	−3.4756	−3.7499	−3.8447	−3.79[b]
InBr	^{115}In	−3.3548	−3.6062	−3.6963	−3.65[b]
InI	^{115}In	−3.2588	−3.4704	−3.5452	−3.49[b]

[a] Ref 65. [b] Ref 66. [c] Ref 67. [d] Ref 68. [e] Ref 69. [f] Ref 70.

Table 13. Calculated Electric Field Gradient, V_{33}, at the Halide Nucleus for a Set of Diatomics, Using the CAM-B3LYP-A Functional

		NR	SR-Z4	Z4	observed
AlCl	^{35}Cl	0.4482	0.4518	0.4519	0.4602[a]
GaCl	^{35}Cl	0.6934	0.7013	0.7019	0.6880[b]
InCl	^{35}Cl	0.7064	0.7260	0.7313	0.6933[b]
CuCl	^{35}Cl	1.8731	2.0695	2.0699	1.675[a]
HCl	^{35}Cl	3.6148	3.6603	3.6610	3.516[c]
ICl	^{35}Cl	4.6548	4.7355	4.7395	4.472[c]
BrCl	^{35}Cl	5.5104	5.5716	5.5730	5.336[c]
AlBr	^{79}Br	1.0249	1.0952	1.1013	1.112[d]
GaBr	^{79}Br	1.4117	1.5007	1.5100	1.50[b]
InBr	^{79}Br	1.4535	1.5625	1.5809	1.57[b]
CuBr	^{79}Br	3.7383	4.3511	4.3777	3.71[e]
HBr	^{79}Br	7.2244	7.6984	7.7394	7.55[c]
IBr	^{79}Br	9.5934	10.2194	10.2786	9.89[b]
BrCl	^{79}Br	12.0816	12.8040	12.8700	12.4[c]
AlI	^{127}I	1.6217	1.9082	1.9727	1.90[b]
GaI	^{127}I	1.9908	2.3116	2.3890	2.28[b]
InI	^{127}I	2.0631	2.4077	2.4989	2.38[b]
TlI	^{127}I	2.0566	2.3743	2.6097	2.70[b]
CuI	^{127}I	5.2757	6.6775	6.8936	5.79[e]
HI	^{127}I	9.9227	11.5014	11.8735	11.3[c]
IBr	^{127}I	15.4910	17.7226	18.2879	16.8[c]
ICl	^{127}I	16.5887	18.9846	19.5867	18.1[c]
IF	^{127}I	19.6142	22.3860	23.1013	21.2[c]
AlF	^{27}Al	−1.1764	−1.1810	−1.1810	−1.096[b]
AlCl	^{27}Al	−0.9828	−0.9849	−0.9849	−0.8828[b]
AlBr	^{27}Al	−0.9170	−0.9124	−0.9123	−0.8130[d]
AlI	^{27}Al	−0.8640	−0.8492	−0.8484	−0.7417[b]
GaF	^{69}Ga	−2.7144	−2.7939	−2.8038	−2.76[b]
GaCl	^{69}Ga	−2.3988	−2.4662	−2.4755	−2.38[f]
GaBr	^{69}Ga	−2.2802	−2.3313	−2.3399	−2.24[b]
GaI	^{69}Ga	−2.1921	−2.2160	−2.2229	−2.10[b]
InF	^{115}In	−3.9160	−4.2220	−4.3274	−4.18[b]
InCl	^{115}In	−3.6177	−3.8945	−3.9977	−3.79[b]
InBr	^{115}In	−3.5026	−3.7544	−3.8555	−3.65[b]
InI	^{115}In	−3.4274	−3.6360	−3.7339	−3.49[b]

[a] Ref 65. [b] Ref 66. [c] Ref 67. [d] Ref 68. [e] Ref 69. [f] Ref 70.

Table 14. Calculated Electric Field Gradient, V_{33}, at the Halide Nucleus for a Set of Diatomics, Using the CAM-B3LYP-B Functional

		NR	SR-Z4	Z4	observed
AlCl	^{35}Cl	0.4555	0.4589	0.4590	0.4602[a]
GaCl	^{35}Cl	0.7111	0.7183	0.7192	0.6880[b]
InCl	^{35}Cl	0.7255	0.7434	0.7488	0.6933[b]
CuCl	^{35}Cl	1.7485	1.9368	1.9371	1.675[a]
HCl	^{35}Cl	3.5972	3.6426	3.6434	3.516[c]

Table 14. Continued

		NR	SR-Z4	Z4	observed
ICl	^{35}Cl	4.6628	4.7393	4.7446	4.472[c]
BrCl	^{35}Cl	5.5378	5.5978	5.5996	5.336[c]
AlBr	^{79}Br	1.0521	1.1228	1.1293	1.112[d]
GaBr	^{79}Br	1.4638	1.5538	1.5636	1.50[b]
InBr	^{79}Br	1.5083	1.6169	1.6359	1.57[b]
CuBr	^{79}Br	3.5011	4.0911	4.1165	3.71[e]
HBr	^{79}Br	7.2211	7.6980	7.7391	7.55[c]
IBr	^{79}Br	9.6806	10.3109	10.3737	9.89[b]
BrCl	^{79}Br	12.2407	12.9805	13.0478	12.4[c]
AlI	^{127}I	1.6956	1.9907	2.0578	1.90[b]
GaI	^{127}I	2.1060	2.4399	2.5217	2.28[b]
InI	^{127}I	2.1794	2.5355	2.6319	2.38[b]
TlI	^{127}I	2.1736	2.4872	2.7337	2.70[b]
CuI	^{127}I	4.9615	6.3195	6.5247	5.79[e]
HI	^{127}I	9.9852	11.5851	11.9611	11.3[c]
IBr	^{127}I	15.7956	18.0980	18.6797	16.8[c]
ICl	^{127}I	16.9230	19.3979	20.0187	18.1[c]
IF	^{127}I	20.0120	22.8680	23.6057	21.2[c]
AlF	^{27}Al	−1.1870	−1.1916	−1.1917	−1.096[b]
AlCl	^{27}Al	−0.9994	−1.0014	−1.0015	−0.8828[b]
AlBr	^{27}Al	−0.9335	−0.9286	−0.9285	−0.8130[d]
AlI	^{27}Al	−0.8821	−0.8662	−0.8654	−0.7417[b]
GaF	^{69}Ga	−2.7589	−2.8390	−2.8492	−2.76[b]
GaCl	^{69}Ga	−2.4573	−2.5249	−2.5344	−2.38[f]
GaBr	^{69}Ga	−2.3381	−2.3882	−2.3970	−2.24[b]
GaI	^{69}Ga	−2.2549	−2.2759	−2.2828	−2.10[b]
InF	^{115}In	−4.0069	−4.3162	−4.4245	−4.18[b]
InCl	^{115}In	−3.7303	−4.0091	−4.1156	−3.79[b]
InBr	^{115}In	−3.6164	−3.8681	−3.9724	−3.65[b]
InI	^{115}In	−3.5525	−3.7573	−3.8582	−3.49[b]

[a] Ref 65. [b] Ref 66. [c] Ref 67. [d] Ref 68. [e] Ref 69. [f] Ref 70.

Table 15. Calculated Electric Field Gradient, V_{33}, at the Halide Nucleus for a Set of Diatomics, Using the CAM-B3LYP* Functional

		NR	SR-Z4	Z4	observed
AlCl	^{35}Cl	0.4972	0.5018	0.5020	0.4602[a]
GaCl	^{35}Cl	0.7389	0.7485	0.7491	0.6880[b]
InCl	^{35}Cl	0.7367	0.7598	0.7651	0.6933[b]
CuCl	^{35}Cl	1.5905	1.7706	1.7710	1.675[a]
HCl	^{35}Cl	3.6640	3.7104	3.7112	3.516[c]
ICl	^{35}Cl	4.7001	4.7869	4.7918	4.472[c]
BrCl	^{35}Cl	5.5935	5.6574	5.6592	5.336[c]
AlBr	^{79}Br	1.1043	1.1836	1.1902	1.112[d]
GaBr	^{79}Br	1.4838	1.5828	1.5926	1.50[b]
InBr	^{79}Br	1.4984	1.6196	1.6384	1.57[b]
CuBr	^{79}Br	3.1880	3.7451	3.7601	3.71[e]
HBr	^{79}Br	7.2972	7.7848	7.8264	7.55[c]
IBr	^{79}Br	9.6872	10.3426	10.4046	9.89[b]
BrCl	^{79}Br	12.2806	13.0320	13.0995	12.4[c]
AlI	^{127}I	1.6993	2.0139	2.0822	1.90[b]
GaI	^{127}I	2.0574	2.4062	2.4873	2.28[b]
InI	^{127}I	2.0975	2.4720	2.5656	2.38[b]
TlI	^{127}I	2.0759	2.4287	2.6726	2.70[b]
CuI	^{127}I	4.5304	5.7966	5.9847	5.79[e]
HI	^{127}I	10.0133	11.6495	12.0283	11.3[c]
IBr	^{127}I	15.7276	18.0668	18.6463	16.8[c]
ICl	^{127}I	16.8661	19.3791	19.9979	18.1[c]
IF	^{127}I	20.0830	23.0210	23.7621	21.2[c]
AlF	^{27}Al	−1.2001	−1.2048	−1.2049	−1.096[b]
AlCl	^{27}Al	−0.9925	−0.9946	−0.9947	−0.8828[b]
AlBr	^{27}Al	−0.9240	−0.9195	−0.9194	−0.8130[d]

Table 15. Continued

		NR	SR-Z4	Z4	observed
AlI	^{27}Al	−0.8671	−0.8520	−0.8512	−0.7417[b]
GaF	^{69}Ga	−2.7718	−2.8543	−2.8644	−2.76[b]
GaCl	^{69}Ga	−2.4221	−2.4903	−2.4995	−2.38[f]
GaBr	^{69}Ga	−2.2949	−2.3461	−2.3547	−2.24[b]
GaI	^{69}Ga	−2.1969	−2.2199	−2.2266	−2.10[b]
InF	^{115}In	−3.9819	−4.3001	−4.4076	−4.18[b]
InCl	^{115}In	−3.6523	−3.9393	−4.0438	−3.79[b]
InBr	^{115}In	−3.5292	−3.7895	−3.8914	−3.65[b]
InI	^{115}In	−3.4438	−3.6586	−3.7568	−3.49[b]

[a] Ref 65. [b] Ref 66. [c] Ref 67. [d] Ref 68. [e] Ref 69. [f] Ref 70.

Note Added after ASAP Publication. This article was published ASAP on August 10, 2010. The title of Table 1 has been modified. The correct version was published on August 19, 2010.

References

(1) Lucken, E. A. C. *Nuclear quadrupole coupling constants*; Academic Press: New York, 1969.

(2) Autschbach, J.; Zheng, S.; Schurko, R. W. *Concepts Magn. Reson. A* **2010**, *36A*, 84–126.

(3) Das, T. P. *Nuclear quadrupole resonance spectroscopy*; Academic Press: New York, 1958.

(4) Dillon, K. B. Nuclear quadrupole resonance spectroscopy. In *Spectroscopic properties of inorganic and organometallic compounds*; The Royal Society of Chemistry: London, 2005; Vol. 37.

(5) Schwerdtfeger, P.; Söhnel, T.; Pernpointner, M.; Laerdahl, J. K.; Wagner, F. E. *J. Chem. Phys.* **2001**, *115*, 5913–5924.

(6) Barone, G.; Mastalerz, G.; Reiher, M.; Lindh, R. *J. Phys. Chem. A* **2008**, *112*, 1666–1672.

(7) Kowalewski, J.; Mäler, L. *Nuclear spin relaxation in liquids: Theory, experiments, and applications*; Taylor & Francis: New York, 2006.

(8) Bryce, D. L.; Eichele, K.; Wasylishen, R. E. *Inorg. Chem.* **2003**, *42*, 5085–5096.

(9) Wong, A.; Pike, K. J.; Jenkins, R.; Clarkson, G. J.; Anupold, T.; Howes, A. P.; Crout, D. H. G.; Samoson, A.; Dupree, R.; Smith, M. E. *J. Phys. Chem. A* **2006**, *110*, 1824–1835.

(10) Bryce, D. L.; Sward, G. D. *Magn. Reson. Chem.* **2006**, *44*, 409–450.

(11) Pernpointner, M.; Visscher, L. *J. Chem. Phys.* **2001**, *114*, 10389.

(12) Visscher, L.; Enevoldsen, T.; Saue, T.; Oddershede, J. *J. Chem. Phys.* **1998**, *109*, 9677–9684.

(13) van Lenthe, E.; Baerends, E. J. *J. Chem. Phys.* **2000**, *112*, 8279–8292.

(14) Neese, F.; Wolf, A.; Fleig, T.; Reiher, M.; Hess, B. A. *J. Chem. Phys.* **2005**, *122*, 204107.

(15) Mastalerz, R.; Barone, G.; Lindh, R.; Reiher, M. *J. Chem. Phys.* **2007**, *127*, 074105.

(16) Rutkowski, A. *J. Phys. B* **1986**, *19*, 149–158.

(17) Rutkowski, A.; Schwarz, W. H. E. *Theor. Chim. Acta* **1990**, *76*, 391–410.

(18) Cazzolia, G.; Puzzarinia, C.; Stopkowicz, S.; Gauss, J. *Mol. Phys.* **2008**, *106*, 1181–1192.

(19) Nichols, P.; Govind, N.; Bylaska, E. J.; de Jong, W. A. *J. Chem. Theory Comput.* **2009**, *5*, 491–499.

(20) Iikura, H.; Tsuneda, T.; Yanai, T.; Hirao, K. *J. Chem. Phys.* **2001**, *115*, 3540–3544.

(21) Yanai, T.; Tew, D. P.; Handy, N. C. *Chem. Phys. Lett.* **2004**, *393*, 51–57.

(22) Livshits, E.; Baer, R. *Phys. Chem. Chem. Phys.* **2007**, *9*, 2932–2941.

(23) Govind, N.; Valiev, M.; Jensen, L.; Kowalski, K. *J. Phys. Chem. A* **2009**, *113*, 6041.

(24) Jensen, L.; Govind, N. *J. Phys. Chem. A* **2009**, *113*, 9761.

(25) Bast, R.; Schwerdtfeger, P. *J. Chem. Phys.* **2003**, *119*, 5988–5994.

(26) van Lenthe, E.; van Lingen, J. N. *Int. J. Quantum Chem.* **2006**, *106*, 2525–2528.

(27) van Lenthe, E.; van der Avoird, A.; Hagen, W. R.; Reijerse, E. J. *J. Phys. Chem. A* **2000**, *104*, 2070–2077.

(28) Faas, S.; van Lenthe, J. H.; Hennum, A. C.; Snijders, J. G. *J. Chem. Phys.* **2000**, *113*, 4052–4059.

(29) Schwarz, W. H. E. Fundamentals of Relativistic Effects in Chemistry. In *The Concept of the Chemical Bond*; Masic, Z. B., Ed.; Springer: Berlin, 1990; Vol. 2, pp 559−643.

(30) Kellö, V.; Sadlej, A. J. *Int. J. Quantum Chem.* **1998**, *68*, 159–174.

(31) Malkin, I.; Malkina, O. L.; Malin, V. G. *Chem. Phys. Lett.* **2002**, *361*, 231–236.

(32) Baerends, E. J.; Schwerdtfeger, P.; Snijders, J. G. *J. Phys. B* **1990**, *23*, 3225–3240.

(33) van Lenthe, E. Ph.D. thesis, Vrije Universiteit Amsterdam, Netherlands, 1996.

(34) Faas, S. Ph.D. thesis, Rijksuniversiteit Groningen, Netherlands, 2000.

(35) Boys, S. F. *Proc. R. Soc. London* **1950**, *200*, 542–554.

(36) King, H. F.; Dupuis, M. *J. Comput. Phys.* **1976**, *21*, 144–165.

(37) Matsuoka, O. *Int. J. Quantum Chem.* **1971**, *5*, 1–11.

(38) Taketa, H.; Huzinaga, S.; O-ohata, K. *J. Phys. Soc. Jpn.* **1966**, *21*, 2313–2324.

(39) Helgaker, T.; Watson, M.; Handy, N. C. *J. Chem. Phys.* **2000**, *113*, 9402–9409.

(40) Dupuis, M. *Comput. Phys. Commun.* **2001**, *134*, 150–166.

(41) Obara, S.; Saika, A. *J. Chem. Phys.* **1986**, *84*, 3963.

(42) Bylaska, E. J. *NWChem*, version 5.1; Pacific Northwest National Laboratory: Richland, WA, 2007.

(43) Kendall, R. A.; Apra, E.; Bernholdt, D. E.; Bylaska, E. J.; Dupuis, M.; Fann, G. I.; Harrison, R. J.; Ju, J.; Nichols, J. A.; Nieplocha, J.; Straatsma, T. P.; Windus, T. L.; Wong, A. T. *Comput. Phys. Commun.* **2000**, *128*, 260–283.

(44) Valiev, M.; Bylaska, E. J.; Govind, N.; Kowalski, K.; Straatsma, T. P.; van Dam, H. J. J.; Wang, D.; Nieplocha, J.; Apra, E.; Windus, T. L.; de Jong, W. A. *Comput. Phys. Commun.* **2010**, *181*, 1477–1489.

(45) Weigend, F.; Ahlrichs, R. *Phys. Chem. Chem. Phys.* **2005**, *7*, 3295–3305.

(46) Feller, D. *J. Comput. Chem.* **2000**, *17*, 1571–1586.

(47) Schuchardt, K.; Didier, B.; Elsethagen, T.; Sun, L.; Gurumoorthi, V.; Chase, J.; Li, J.; Windus, T. *J. Chem. Inf.* **2007**, *47*, 1045–1052.

(48) Belanzoni, P.; Baerends, E.; van Lenthe, E. *Mol. Phys.* **2005**, *103*, 775–787.

(49) Tsuchiya, T.; Abe, M.; Nakajima, T.; Hirao, K. *J. Chem. Phys.* **2001**, *115*, 4463–4472.

(50) Pantazis, D. A.; Neese, F. *J. Chem. Theory Comput.* **2009**, *5*, 2229–2238.

(51) Roos, B. O.; Lindh, R.; Malmqvist, P.; Veryazov, V.; Widmark, P. *J. Phys. Chem. A* **2005**, *109*, 6575–6579.

(52) Becke, A. D. *Phys. Rev. A* **1988**, *38*, 3098–3100.

(53) Perdew, J. P. *Phys. Rev. B* **1986**, *33*, 8822–8824.

(54) Lee, C.; Yang, W.; Parr, R. G. *Phys. Rev. B* **1988**, *37*, 785–789.

(55) Becke, A. D. *J. Chem. Phys.* **1993**, *98*, 1372–1377.

(56) Thierfelder, C.; Schwerdtfeger, P.; Saue, T. *Phys. Rev. A* **2007**, *76*, 034502−4.

(57) Perdew, J. P.; Burke, K.; Ernzerhof, M. *Phys. Rev. Lett.* **1996**, *77*, 3865–3868.

(58) Perdew, J. P.; Burke, K.; Ernzerhof, M. *Phys. Rev. Lett.* **1997**, *78*, 1396.

(59) Zhang, Y.; Yang, W. *Phys. Rev. Lett.* **1998**, *80*, 890.

(60) Glendening, E. D.; Badenhoop, J. K.; Reed, A. E.; Carpenter, J. E.; Bohmann, J. A.; Morales, C. M.; Weinhold, F. *NBO 5.0*; Theoretical Chemistry Institute, University of Wisconsin: Madison, WI, 2001. http://www.chem.wisc.edu/∼nbo 5 (accessed July 2010).

(61) Ye, A.; Autschbach, J. *J. Chem. Phys.* **2006**, *125*, 234101–13.

(62) Autschbach, J.; Zheng, S. *Magn. Reson. Chem.* **2008**, *46*, S48–S55.

(63) van Wullen, C. *J. Chem. Phys.* **1998**, *109*, 392–399.

(64) Philipsen, P. H. T.; van Lenthe, E.; Snijders, J. G.; Baerends, E. J. *Phys. Rev. B* **1997**, *56*, 13556–13562.

(65) Hensel, K. D.; Styger, C.; Jager, W.; Merer, A. J.; Gerry, M. C. L. *J. Chem. Phys.* **1993**, *99*, 3320–3328.

(66) Lucken, E. A. C. In *Advances in Nuclear Quadrupole Resonance*; Smith, J. A. S., Ed.; Wiley: New York, 1983; Vol. 5, pp 83–124.

(67) Palmer, M. H. *Naturforsch. A* **1998**, *53*, 615.

(68) Walker, K. A.; Gerry, M. C. *J. Mol. Spectrosc.* **1999**, *193*, 224–227.

(69) Sheridan, J. In *Advances in Nuclear Quadrupole Resonance*; Smith, J. A. S., Ed.; Wiley: New York, 1983; Vol. 5, pp 125–163.

(70) Gordy, W.; Cook, R. L. *Microwave Molecular Spectra*; Wiley: New York, 1984; pp 859−872.

(71) Pyykkö, P. *Mol. Phys.* **2008**, *106*, 1965–1974.

(72) Schwerdtfeger, P.; Pernpointner, M.; Nazarewicz, W. Calculation of nuclear quadrupole coupling constants. In *Calculation of NMR and EPR parameters: Theory and applications*; Kaupp, M., Bühl, M., Malkin, V. G., Eds.; Wiley-VCH: Weinheim, Germany, 2004; pp 279−291.

(73) Schwerdtfeger, P.; Bast, R.; Gerry, M. C. L.; Jacob, C. R.; Jansen, M.; Kellö, V.; Mudring, A. V.; Sadlej, A. J.; Saue, T.; Söhnel, T.; Wagner, F. E. *J. Chem. Phys.* **2005**, *122*, 124317.

(74) Schwerdtfeger, P.; Pernpointner, M.; Laerdahl, J. K. *J. Chem. Phys.* **1999**, *111*, 3357–3364.

(75) Townes, C. H.; Dailey, B. P. *J. Chem. Phys.* **1949**, *17*, 782–796.

(76) Szilagyi, R. K.; Metz, M.; Solomon, E. *J. Phys. Chem. A* **2002**, *106*, 2994–3007.

(77) Sanderson, C. T.; Palmer, B. J.; Morgan, A.; Murphy, M.; Dluhy, R. A.; Mize, T.; Amster, I. J.; Kutal, C. *Macromolecules* **2002**, *35*, 9648–9652.

(78) Bard, A. J.; Fox, M. A. *Acc. Chem. Res.* **1995**, *28*, 141–145.

(79) Hara, M.; Waraksa, C. C.; Lean, J. T.; Lewis, B. A.; Mallouk, T. E. *J. Phys. Chem. A* **2000**, *104*, 5275–5280.

(80) Gao, F. G.; Bard, A. J. *J. Am. Chem. Soc.* **2000**, *122*, 7426–7427.

(81) Hagfeldt, A.; Graetzel, M. *Chem. Rev.* **1995**, *95*, 49–68.

(82) Klimant, I.; Wolfbeis, O. S. *Anal. Chem.* **1995**, *67*, 3160–3166.

(83) Erkkila, K. E.; Odom, D. T.; Barton, J. K. *Chem. Rev.* **1999**, *99*, 2777–2795.

(84) Armistead, P. M.; Thorp, H. H. *Bioconjugate Chem.* **2002**, *13*, 172–176.

(85) Kirsch-De Mesmaeker, A.; Lecomte, J. P.; Kelly, J. M. *Top. Curr. Chem.* **1996**, *177*, 25–76.

(86) Barton, J. K. *Science* **1986**, *233*, 727–734.

(87) Sundquist, W. I.; Lippard, S. J. *Coord. Chem. Rev.* **1990**, *100*, 293–322.

(88) Pauly, M.; Kayser, I.; Schmitz, M.; Dicato, M.; Del Guerzo, A.; Kolber, I.; Moucheron, C.; Kirsch-De Mesmaeker, A. *Chem. Commun.* **2002**, *108*, 6–1087.

(89) Pourtois, G.; Belionne, D.; Moucheron, C.; Schumm, S.; Kirsch-De Mesmaeker, A.; Lazzaroni, R.; Bredas, J.-L. *J. Am. Chem. Soc.* **2004**, *126*, 683–692.

(90) Bechthold, H.; Rehder, D. *J. Organomet. Chem.* **1981**, *206*, 305–315.

(91) Bühl, M.; Gaemers, S.; Elsevier, C. J. *Chem.—Eur. J.* **2000**, *6*, 3272–3280.

(92) Wagner, F. E.; Wagner, U. *Mössbauer Isomer Shifts*, 1st ed.; Shenoy, G. K., Wagner, F. E., Eds.; North Holland: Amsterdam, 1978; pp 431−514.

(93) Lo, A. Y. H.; Bitterwolf, T. E.; Macdonald, C. L. B.; Schurko, R. W. *J. Phys. Chem. A* **2005**, *109*, 7073–7087.

(94) Schreckenbach, G.; Shamov, G. A. *Acc. Chem. Res.* **2010**, *43*, 19–29.

(95) Cho, H.; de Jong, W. A.; Soderquist, C. Z. *J. Chem. Phys.* **2010**, *132*, 084501.

(96) Pepper, M.; Bursten, B. E. *Chem. Rev. B* **1991**, *91*, 719–741.

(97) Clark, D. L.; Hobart, D. E.; Neu, M. P. *Chem. Rev.* **1995**, *95*, 25–48.

(98) de Jong, W. A.; Visscher, L.; Nieuwpoort, W. C. *J. Mol. Struct.* **1998**, *458*, 41–52.

(99) Monard, J. A.; Huray, P. G.; Thomson, J. O. *Phys. Rev. B* **1974**, *9*, 2838–2845.

(100) Larsson, S.; Pyykkö, P. *Chem. Phys.* **1986**, *101*, 355.

(101) Pyykkö, P.; Seth, M. *Theor. Chem. Acc.* **1997**, *96*, 92.

CT1002847